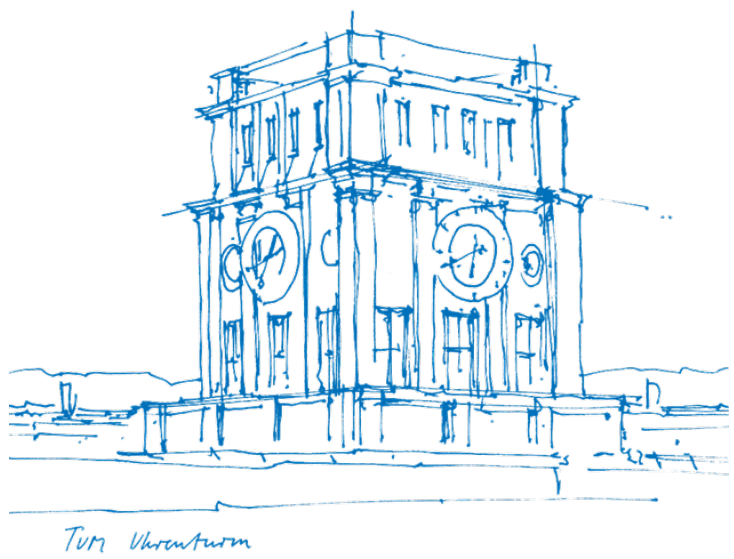


DORIS-Based Ionospheric Corrections for Single-Frequency Radar Altimetry

Ke Zhang



DORIS-Based Ionospheric Corrections for Single-Frequency Radar Altimetry

Ke Zhang

DORIS-Based Ionospheric Corrections for Single-Frequency Radar Altimetry

Ke Zhang

Thesis for the attainment of the academic degree

Master of Science (M.Sc.)

at the TUM School of Engineering and Design of the Technical University of Munich.

Examiner: Schmidt Michael; Apl. Prof. Dr.-Ing. habil.

Supervisor: Schmidt Michael; Apl. Prof. Dr.-Ing. habil.

Submitted:

Munich, 03.12.2024

I hereby declare that this thesis is entirely the result of my own work except where otherwise indicated. I have only used the resources given in the list of references.

Abstract

The ionosphere is a component of Earth's atmosphere, spanning an altitude range from 50 km to 1000 km. The ionosphere contains numerous charged particles and free electrons due to the influence of ultraviolet radiation emitted by the Sun, and the activity level of the ionosphere is also closely related to the Sun's activity. The year 2024 marks a peak in the solar activity cycle, during which ionospheric storms (in May 2024) caused by solar flares exerted stress on electric power grids and disturbance radio communication. Additionally, electromagnetic signals passing through the ionosphere experience ionospheric delay related to their frequency and ionospheric activity condition, which could reach several meters and must be corrected. These facts highlight that monitoring the ionosphere is necessary for satellite-based communication, positioning, and other related applications. This thesis aims to monitor the ionosphere with Doppler Orbitography and Radiopositioning Integrated by Satellite (DORIS) system and to provide ionospheric corrections for single-frequency radar altimetry.

The initial purpose of the DORIS system was to provide Precise Orbit Determination (POD) services for Low Earth Orbit (LEO) satellites. However, it is also well-suited for observation of electron density in the Earth's ionosphere. DORIS transmits signals using two frequencies in the L-band, and the signals are transmitted from the ground station to the receiver onboard the satellite. Given that DORIS ground stations are distributed uniformly worldwide, and modern DORIS receivers can simultaneously receive signals from different stations and frequencies, it is highly suitable to use DORIS to monitor the vertical total electron content (VTEC) of the ionosphere.

Moreover, the DORIS system is widely deployed on altimetry satellites, and similar observational conditions for DORIS and altimetry signals mean that they have comparable ionospheric conditions. Consequently, it is feasible for DORIS to provide ionospheric corrections for altimetry observations. In this thesis, DORIS-based altimetry VTEC (correction for altimetry) is computed by pre-selection and interpolating DORIS VTEC at altimetry Ionospheric Piercing Point (IPP). Two selection strategies for DORIS VTEC — time division and space division — were compared. These strategies are based on the time interval and spatial window near the altimetry IPP, respectively. Under the premise of achieving 50% coverage of altimetry IPPs, the space division outperformed the time division with slightly higher accuracy (0.1 TECU under active ionospheric conditions). No significant difference was observed in interpolation methods between Inverse Distance Weighting (IDW) and Kriging.

After obtaining the DORIS-based altimetry VTEC, this thesis compared it with the GIM-based altimetry VTEC, which is obtained by direct interpolation of GIM at the altimetry IPP. Results show that, during quiet ionospheric periods, the DORIS-based altimetry VTEC has an average accuracy advantage of 0.1 TECU over a 30-day period. During active ionospheric periods, the GIM-based altimetry VTEC outperforms the DORIS-based altimetry VTEC, with an accuracy advantage of 0.5 TECU.

Overall, during periods of low ionospheric activity, DORIS can provide a certain improvement in accuracy compared to GIM, making it suitable for ionospheric correction of single-frequency altimetry. However, under conditions of high ionospheric activity, the performance of DORIS corrections is inferior to that of GIM products. Employing a more optimized data selection strategy or combining DORIS with GIM products could be potential approaches to improve the accuracy of ionospheric corrections for single-frequency radar altimetry.

Contents

| | |
|---|-----------|
| Abstract | ix |
| 1 Introduction | 1 |
| 1.1 Background | 1 |
| 1.2 Research Status | 2 |
| 1.3 Significance of the Study | 3 |
| 1.4 Content of the Study | 4 |
| 2 Ionosphere | 5 |
| 2.1 Impact of Solar Activity on the Earth's Ionosphere | 5 |
| 2.2 Ionospheric Impact on Electromagnetic Wave Signals | 7 |
| 2.3 Parameterization of Ionospheric Delay | 8 |
| 2.3.1 Derivation of Electron Density | 8 |
| 2.3.2 Mapping Function | 10 |
| 2.4 Existing Ionosphere Models | 11 |
| 2.5 Summary of the Chapter | 12 |
| 3 Satellite Altimetry | 13 |
| 3.1 Observation Equation of Satellite Altimetry | 13 |
| 3.2 Altimetry Mission: Introduction of Jason-3 | 15 |
| 3.3 Summary of the Chapter | 15 |
| 4 DORIS | 17 |
| 4.1 Ground and Satellite Segments | 17 |
| 4.2 DORIS Data processing | 18 |
| 4.2.1 Types of DORIS Observations | 18 |
| 4.2.2 Observation Equation of DORIS | 19 |
| 4.2.3 Derivation of DORIS STEC | 19 |
| 4.3 Summary of the Chapter | 21 |
| 5 Methods: From DORIS STEC to DORIS-based Altimetry VTEC | 23 |
| 5.1 DORIS STEC Leveling | 23 |
| 5.2 DORIS-based Altimetry VTEC Derivation from DORIS VTEC | 26 |
| 5.2.1 Data Preprocessing | 26 |
| 5.2.2 Data Interpolation | 27 |
| 5.3 Summary of the Chapter | 29 |
| 6 Results and Analysis | 31 |
| 6.1 DORIS STEC: Leveling | 31 |
| 6.2 DORIS-based Altimetry VTEC: Data Preprocessing | 34 |
| 6.2.1 Data Used for Parameter Evaluation | 35 |
| 6.2.2 Elevation Mask | 36 |
| 6.2.3 Parameters in Space Division | 38 |
| 6.2.4 Parameters in Time Division | 42 |

| | | |
|---------------------|---|-----------|
| 6.2.5 | Comparison of Two Division Strategies | 45 |
| 6.3 | DORIS-based Altimetry VTEC: Interpolation | 46 |
| 6.4 | DORIS-based altimetry VTEC: Comparison with GIM | 47 |
| 6.5 | Summary of the Chapter | 52 |
| 7 | Summary and Outlook | 53 |
| Bibliography | | 57 |

1 Introduction

1.1 Background

Radar altimetry is a remote sensing technique that measures the height of the Earth's surface. Running in a low earth orbit (LEO), the satellite attains ground height information by recording the travel time of electromagnetic signals. In the measuring process, the onboard antenna sends radar pulses to the earth's surface in nadir direction, and the signals are reflected by the water or ice surface and finally received by the sensors onboard the spacecraft. Roughly speaking, the distance between the earth's surface and the spacecraft is computed by the propagation time of the pulses, and the height of the surface can be derived by subtracting the spacecraft's height from the distance. Radar altimetry has been widely used to monitor sea level changes, polar ice melt, and land hydrology by providing accurate and consistent elevation data. It has become an indispensable part of climate research, natural disaster management, and environmental monitoring.

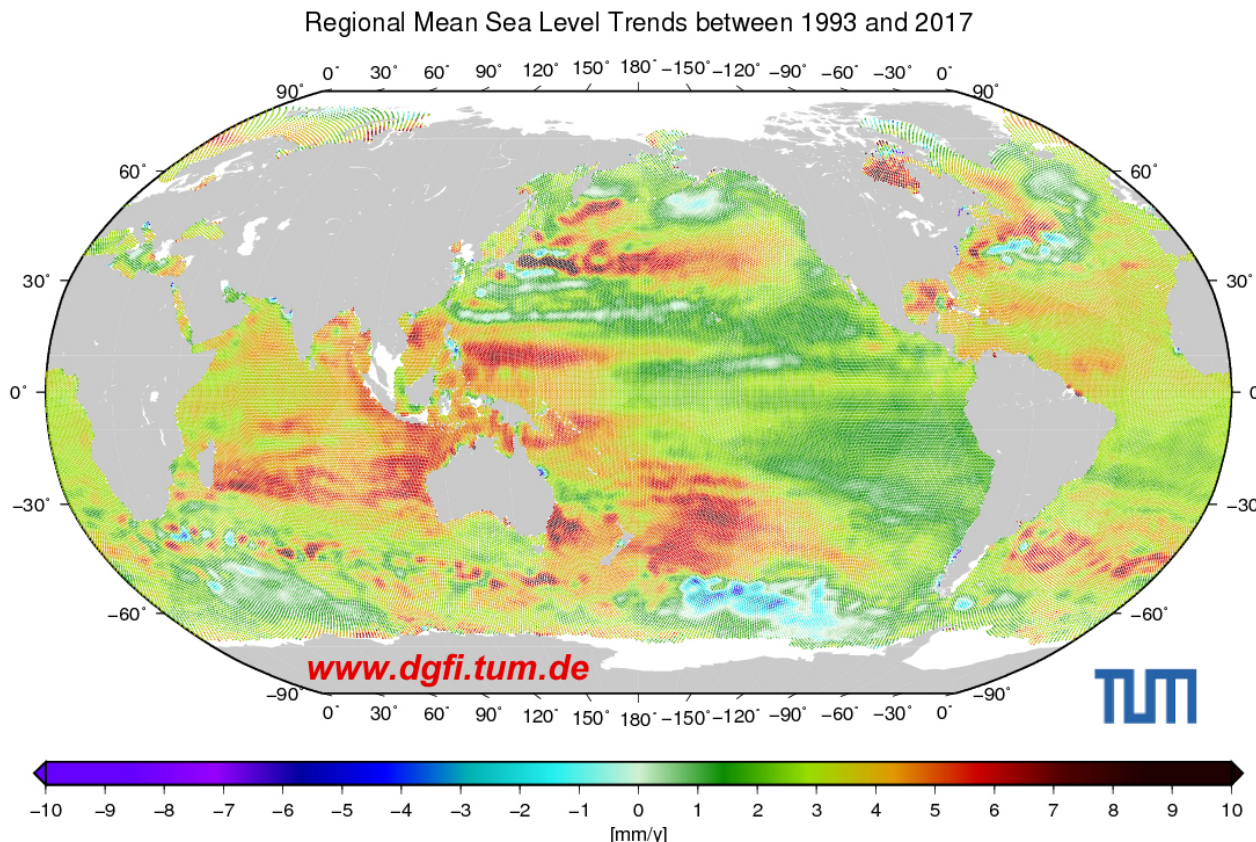


Figure 1.1 Regional Mean Sea Level Trends between 1993 and 2017, Source: Deutsches Geodätisches Forschungsinstitut (DGFI-TUM), <https://www.dgfi.tum.de>

Although the principle of radar altimetry is not complicated, the applications of the technique impose high accuracy requirements on the measurement system. Figure 1.1 shows the Global Mean Sea Level (GMSL) changes from 1993 to 2017. The average variation of GMSL on a global scale is only in the order of 3

mm per year [9]. Therefore, accurate acquisition of satellite orbit position and careful consideration of error sources in altimetry measurement are necessary to meet the requirements of its applications.

Among the various factors influencing the propagation of radar pulses, the ionosphere plays an important role. The ionosphere is an atmosphere layer covering a height of 50-1000 km, where free electrons and ions are produced by the ionization of atmospheric gases. As the pulses travel through the ionosphere, the interaction between the pulses and ionosphere particles (mostly free electrons) changes both the speed and the path of the pulses. As a dispersive medium, the ionosphere imposes delay and bending on signals that are inversely proportional to the square of their frequency. Therefore, under identical observational conditions, a combination of observations from different frequencies allows for an effective elimination of ionospheric delay effects. However, for single-frequency electromagnetic signals, eliminating the effects of ionospheric delay requires the assistance of external models.

On the other hand, obtaining precise satellite positioning, i.e. Precise Orbit Determination (POD), requires the assistance of techniques such as Satellite Laser Ranging (SLR), Doppler Orbitography and Radiopositioning Integrated by Satellite (DORIS), and Global Navigation Satellite System (GNSS). Among these, DORIS has been widely integrated into altimetry satellites for over 30 years. It is a satellite-based positioning system that determines the precise location of satellites in orbit by measuring the Doppler shift of radio signals transmitted between ground beacons and the satellite. Communicating via electromagnetic signals, DORIS is also subject to ionospheric delay during signal propagation. Considering that the DORIS system on the satellite requires at least dual-frequency signals to calculate the Doppler shift, and its widespread use in altimetry satellite missions, utilizing dual-frequency DORIS signals for ionospheric correction computation provides a viable approach for correction of single-frequency altimetry observations.

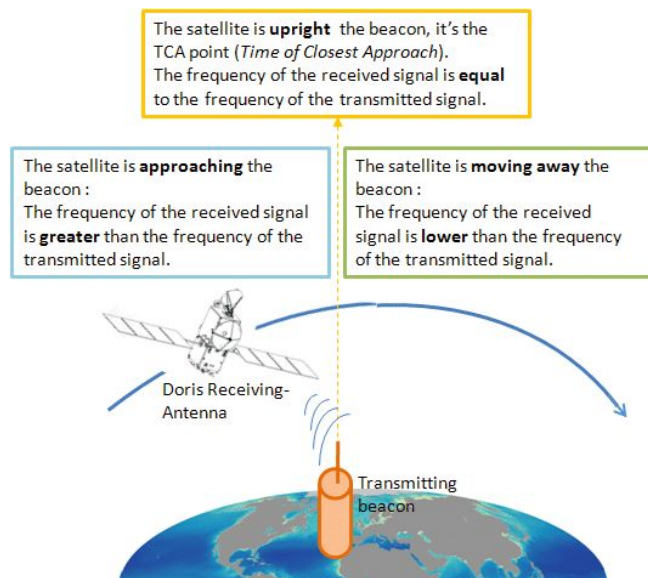


Figure 1.2 Principle of DORIS measurements, Source: Archiving, Validation and Interpretation of Satellite Oceanographic data (AVISO+), <https://www.aviso.altimetry.fr/>

1.2 Research Status

Due to the complexity of the ionospheric structure, it is necessary to conduct in-depth research into the mechanisms governing ionospheric behavior. Significant efforts have been devoted to observing and investigating the patterns of the ionosphere, to identify effective methods to mitigate its impact on electromagnetic signal propagation.

Currently, two types of models are generated to describe ionospheric delay on signals: empirical-driven models and data-driven models. Empirical models rely on historical data to establish relationships between observed parameters and ionospheric activities. Examples of these models include the Klobuchar model [16], the NeQuick model [27], the International Reference Ionosphere (IRI) model [5], the BDGIM [38] and other. However, due to the complexity of the ionospheric structure and the variability of solar activity, such models are not always capable of providing highly accurate ionospheric corrections. Therefore, data-driven models have gained growing importance over the years. For these models, the modeling of the ionospheric delay is based on real-time or near real-time observational data, and they can provide higher accuracy even in periods with anomalous events such as solar storms [7]. Most data-driven models utilize GNSS data, for instance from the global positioning system (GPS) system. Among them, the most cited one is the global ionosphere map (GIM) released by the International GNSS Service (IGS) [10].

However, obtaining the activity of the ionosphere does not solely depend on GNSS systems. Theoretically, observational data from any system providing more than two frequencies can be used to attain information on the ionospheric delay of signals. Radio Occultation (RO) utilizes signals between occulting GNSS satellites and LEO satellites to study vertical profiles of the ionosphere [1]. Dual frequency altimetry observations provide information on the horizontal ionospheric variations [21], and some researchers have combined multiple ionospheric observation methods, including terrestrial GPS, space-based GPS, altimetry, and VLBI, achieving higher accuracy compared to using individual methods alone [30] [8].

In addition, another space-geodesy technology can also obtain information on the ionosphere - DORIS. For more than 30 years DORIS observations have been exploited to examine the ionosphere characteristics. In 2007, Li and Parrot utilized DORIS to study the ionospheric variations caused by seismic waves [19]. Entering the 2010s, more satellite missions equipped with DORIS were launched with improved signal receivers onboard [2]. Additionally, the data exchange format for DORIS became standardized, and the number of ground-based DORIS stations increased. Dettmering et al. used satellites equipped with the DORIS system to model VTEC (Vertical Total Electron Content), an index describing ionospheric activity, and achieved an accuracy comparable to existing models [7]. Liu explores the possibility of utilizing DORIS as an independent reference for validating GNSS-based ionosphere maps [22]. Limberger integrated observations from DORIS, RO, GNSS, and RA data to explore the construction of ionospheric models using B-spline techniques [21].

1.3 Significance of the Study

As an important component of Earth's atmosphere, the ionosphere substantially impacts the propagation of electromagnetic signals, making it one of the key sources of error in satellite communication and navigation applications. Whereas ionosphere-free combinations can be formed for dual-frequency observations, effective ionospheric correction must be applied to achieve accurate altimetry measurements for single-frequency altimetry data.

The Global Ionosphere Maps (GIM), which utilize GNSS data, are the most prominent models that provide information about ionospheric delay on a global scale. GIM offers ionospheric correction in a spatial resolution of 2.5° (latitude) \times 5° (longitude) and a temporal resolution of two hours. The correction accuracy at grid points is approximately 2 TECU, but this accuracy significantly decreases at interpolation points. Moreover, since GNSS receivers are predominantly located on land, there is a sparse density of ionospheric observations over oceanic regions. Given these limitations, relying solely on GIM products may not be the most effective approach for the correction of ionospheric delay.

On the other hand, this study investigates the potential of leveraging DORIS signals for ionospheric correction of single-frequency altimetry observations. Compared to GNSS, DORIS signals feature a larger frequency difference between their dual-frequency components, theoretically enabling a more accurate

ionospheric delay characterization. Additionally, DORIS systems are commonly integrated into altimetry satellites, meaning that DORIS observations are directly collected within the same platform. Moreover, DORIS receivers are also deployed across various types of satellite missions as a POD tool. This implies that utilizing DORIS to provide ionospheric delay information has a wide range of applications.

1.4 Content of the Study

This thesis explores the feasibility, methodology, and accuracy of using DORIS to provide ionospheric corrections for altimetry satellites. For comparison purposes, Jason-3, a satellite equipped with both dual-frequency DORIS and altimetry receivers, will be used as the data source. Specifically, the study will first investigate the method of deriving DORIS VTEC from dual-frequency DORIS observations. Subsequently, DORIS VTEC will be employed to attain interpolated DORIS-based altimetry VTEC at the altimetry IPP locations. In this process, different parameters will be examined to achieve the optimal interpolation results. Finally, the DORIS-based altimetry VTEC will be compared against the dual-frequency altimetry VTEC, considered as the ground truth, to evaluate the accuracy of the DORIS correction. The contents of the seven chapters of this thesis are as follows:

The first chapter provides an overview of radar altimetry, the ionosphere, and DORIS, emphasizing the importance of the thesis and summarizing its core content.

Chapter 2 explores the relationship between solar activity and variations in ionospheric conditions. It details the methodology for calculating the signal delay caused by the ionosphere and introduces ionospheric activity indices involving VTEC and IPP for parameterized descriptions.

The third chapter focuses on the DORIS instruments aboard satellites and their corresponding ground stations. It also explains the DORIS observation equations and outlines the procedures for generating unleveled DORIS STEC values.

Chapter 4 introduces altimetry observation techniques, the process of extracting altimetry VTEC, and the primary data source for this study, Jason-3.

Chapter 5 describes the methodology of the thesis, including the use of GIM for leveling DORIS STEC (Slant Total Electron Content), the steps involved in deriving DORIS VTEC from DORIS STEC, and the preprocessing and interpolation techniques required to obtain DORIS-derived altimetry VTEC from DORIS VTEC.

In the sixth chapter, the results derived from the methods discussed in Chapter 5 are presented. This chapter includes a comparison between leveled DORIS STEC and corresponding GIM STEC and a comparison of DORIS-based altimetry VTEC with dual-frequency altimetry VTEC. Additionally, it evaluates the effectiveness of various preprocessing and interpolation techniques under quiet and active ionospheric conditions to arrive at a more representative conclusion.

Chapter 7 provides a summary and future perspectives, identifying areas for improvement based on the findings in Chapter 6. It suggests further research to enhance the accuracy of DORIS-based altimetry VTEC and improve corrections for single-frequency altimetry satellites.

The code used in this thesis was written by the author using Python, with parts converted from C++ in the OPTIMAP software developed by DGFI¹. The source code and related documentations are available at <https://github.com/AlexZhang0220/DORIS-based-altimetry-VTEC>.

¹<https://www.dgfi.tum.de/en/projects/optimap/>

2 Ionosphere

The ionosphere is a region formed by the ionization of molecules and atoms in the Earth's upper atmosphere under ultraviolet radiation. It consists of free electrons and positive and negative ions, but when viewed on a macroscopic scale, it remains a neutral plasma region. Occupying an altitude range of 50 to 1000 km, the Earth's ionosphere is one of the major sources of error in the propagation of electromagnetic signals.

This chapter will introduce the impact of the Sun on the ionosphere, describe the indices used to measure solar activity, explain the effect of free electrons in the ionosphere on electromagnetic signal propagation, and outline methods for quantifying this impact.

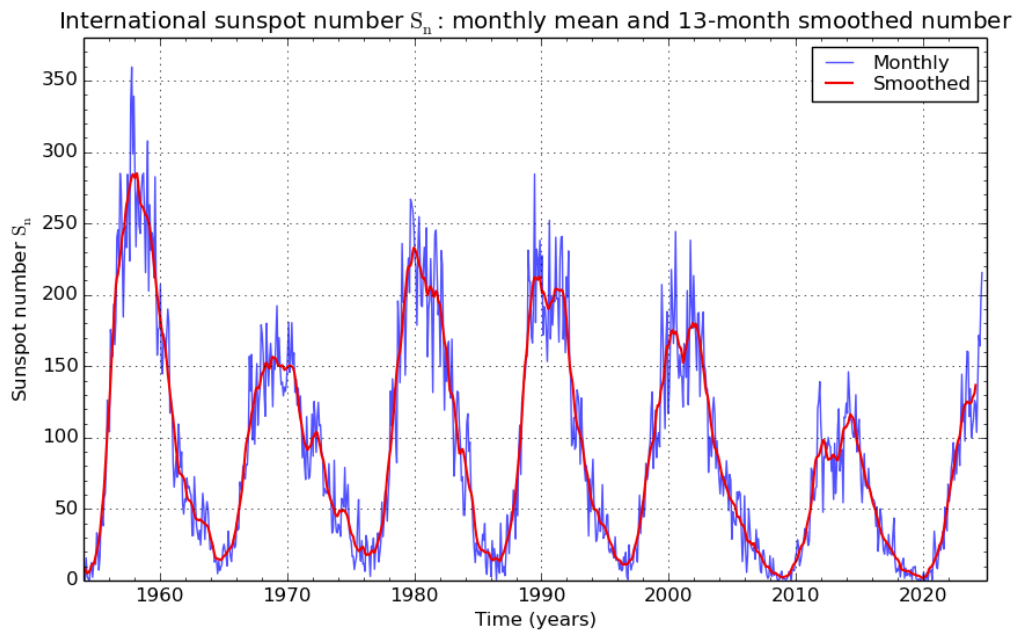
2.1 Impact of Solar Activity on the Earth's Ionosphere

The Sun is the closest star to the Earth, located one astronomical unit¹ away. The Sun contributes the largest portion of ultraviolet radiation that the Earth receives and is the primary driver of ionization in the Earth's atmosphere. The ultraviolet radiation emitted by the Sun primarily originates from its outer layers, namely the photosphere and the corona. The photosphere, with a temperature of approximately 5,500 degrees Celsius, emits significant ultraviolet radiation due to its high thermal energy. At the same time, the most intense ultraviolet radiation is produced by the corona, the Sun's outermost atmospheric layer, which reaches temperatures of several million degrees Celsius. The extremely high temperature and low density of the corona facilitate the emission of ultraviolet and X-ray radiation, contributing to the Sun's overall ultraviolet radiation.

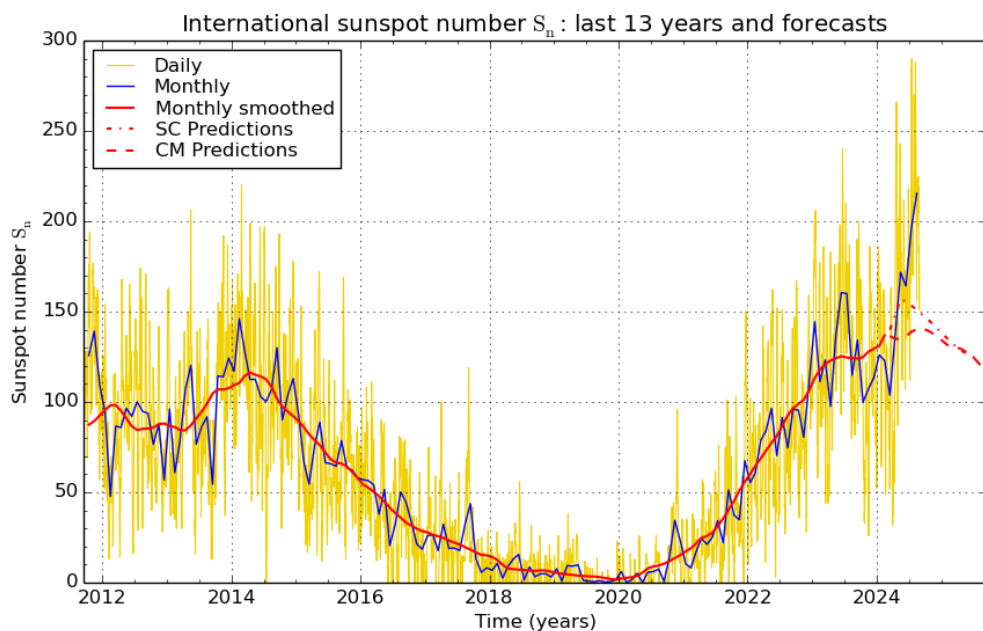
The intensity of solar activity is closely related to the number of sunspots. Sunspots are relatively dark regions on the solar surface formed due to the complex dynamics of the solar magnetic field. The quantity and size of sunspots exhibit a close relationship with the solar activity cycle. During periods of high solar activity, the number of sunspots increases significantly. This increase reflects a more intense solar magnetic activity, which is often accompanied by phenomena such as solar flares and coronal mass ejections. Conversely, during periods of reduced solar activity, the number of sunspots diminishes, indicating a quiet solar state with reduced magnetic activity.

Figure 2.1 illustrates the variation of sunspot numbers in two different time scales. The left figure shows the fluctuation over sixty years, where the 11-year Sun activity cycle can be spotted. The right figure illustrates the variation in the number of sunspots over the past 13 years, along with predictions of one year from sunspot trends only (SC predictions) and also considering the geomagnetic index (CM predictions). The figure shows that the number of sunspots in the current cycle reached its lowest point around 2020 and its highest point around 2024, with overall activity being more intense compared to the previous cycle. The monitoring of sunspot variations provides valuable insights into the overall solar activity and its implications for space weather phenomena affecting the Earth's ionosphere.

¹1AU = 149,597,870,700 m



SILSO graphics (<http://sidc.be/silso>) Royal Observatory of Belgium 2024 September 1



SILSO graphics (<http://sidc.be/silso>) Royal Observatory of Belgium 2024 September 1

Figure 2.1 Variation of sunspot number in sixty years and twelve years, source: Sunspot Index and Long-term Solar Observations (SILSO), <http://www.sidc.be>

Another index used to describe the intensity of solar radiation is the F10.7 index. Unlike the sunspot number, the F10.7 index represents the flux density of solar radiation received by the Earth. This index has a long history of observational data, spanning several decades, which allows for the analysis of trends in solar behavior. Figure 2.2 illustrates the variation of the F10.7 index for the last decade, and from the comparison with Figure 2.1(b) we can see that there is a strong correlation between the fluctuation of sunspot numbers and the F10.7 index. Moreover, the fact that the F10.7 index measures solar radiation that reaches the Earth makes it a more accurate reflection of the impact of solar radiation on the Earth's ionosphere.

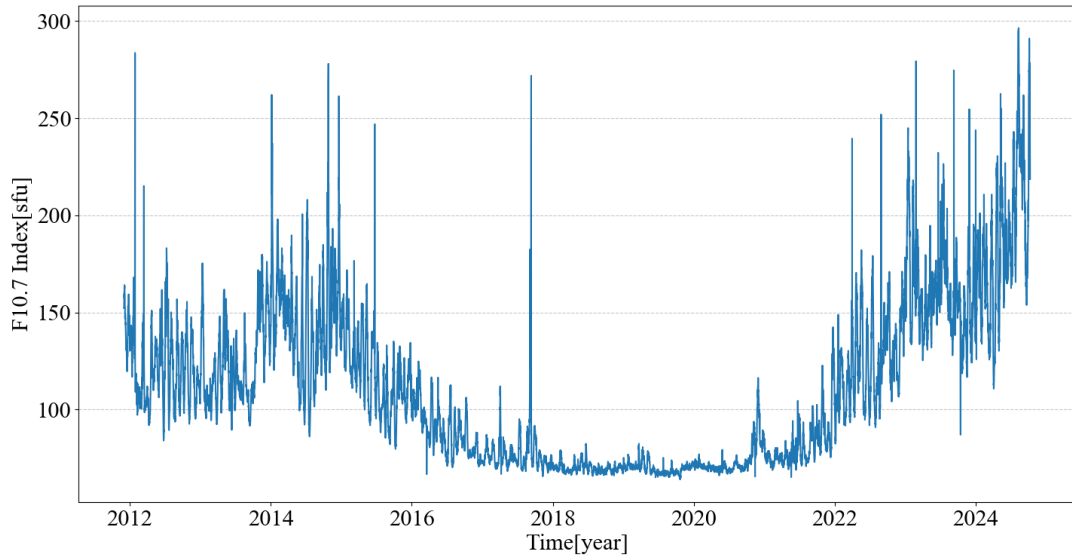


Figure 2.2 Variation of F10.7 Index between 2012 and 2024, source: <https://spaceweather.gc.ca>

2.2 Ionospheric Impact on Electromagnetic Wave Signals

When electromagnetic waves pass through the ionosphere, their propagation speed will be changed by the influence of the free electrons depending on the signal frequency [17]. Consequently, the theoretical distance calculated by multiplying the signal travel time by the speed of light in vacuum differs from the geometric distance between the signal transmitter and the receiver. In this section, the magnitude of the changed distance on signals (the ionospheric delay) will be derived.

The phase velocity of electromagnetic wave signals v_p in a given medium is related to the phase refractive index n_p of that medium relative to a vacuum.

$$v_p = \frac{c}{n_p} \quad (2.1)$$

In Equation (2.1) c is the speed of light in a vacuum. The relationship between the phase refractive index and the electron density of the ionosphere can be described by Equation (2.2) [20]:

$$n_p = 1 - \frac{N_e K_1}{f^2} \pm \frac{N_e K_2 H_0 \cos\theta}{f^3} - \frac{N_e K_3}{f^4} \quad (2.2)$$

where

$$\left\{ \begin{array}{l} K_1 = \frac{e^2}{8\pi^2 \epsilon_0 m} \\ K_2 = \frac{\mu_0 e^3}{16\pi^3 \epsilon_0 m^2} \\ K_3 = \frac{e}{128\pi^4 \epsilon_0^2 m^2} \end{array} \right. \quad (2.3)$$

In the equations, N_e is the electron density, commonly expressed as electrons/m³ or electrons/cm³, ϵ_0 is the permittivity of free space, e is the elementary charge of an electron, m_e is the mass of an electron, f is the frequency of the signal, H_0 is the magnetic field strength of the geomagnetic field, θ is the angle between the direction of the geomagnetic field and the propagation direction of the electromagnetic wave.

For signals with frequency higher than 100MHz, the impact of the K_2 term in Equation (2.2) is smaller than 1% of the total delay, and smaller for the K_3 term [29]. Therefore, in this thesis only the first two terms are considered:

$$n_p = 1 - K_1 \frac{N_e}{f^2} = 1 - 40.3 \frac{N_e}{f^2} \quad (2.4)$$

Combining Equation 2.4) with Equation (2.1) and considering that the last term in Equation (2.4) above has a very small value for high-frequency signals, we can make the following approximation to obtain the phase velocity of the signal:

$$v_p = \frac{c}{n_p} = \frac{c}{1 - 40.3 \frac{N_e}{f^2}} = c \left(1 + 40.3 \frac{N_e}{f^2} \right) \quad (2.5)$$

From Equation (2.5), it can be seen that the phase velocity of electromagnetic wave propagates faster compared to its speed in a vacuum, and this change is directly related to its frequency f and the electron density N_e along the propagation path.

It is important to note that v_p in the equations above is not the material propagation speed of the signal, but rather the phase velocity of the electromagnetic wave in the ionosphere. Additionally, for a set of electromagnetic wave signals with different frequencies, the overall propagation speed in the ionosphere is referred to as the group velocity v_g , and this speed is slightly lower than the material propagation speed. For DORIS signals, the carrier phase component of the signal travels at the phase velocity, and the pseudorange code component propagates at the group velocity. This thesis primarily investigates ionospheric corrections through carrier phase measurements, so the following discussion will focus on deriving the ionospheric delay for the carrier phase with phase velocity v_p .

Outside the ionosphere where the electron density $N_e = 0$, the signal propagates approximately at the speed of light c in vacuum (here tropospheric delay is not considered). If the propagation time between the satellite and the ground station is Δt , then the geometric distance ρ from the satellite to the receiver is given by:

$$\begin{aligned} \rho &= \int_{\Delta t} v_g dt = \int_{\Delta t} (c + c \cdot 40.3 \frac{N_e}{f^2}) dt \\ &= c \cdot \Delta t + \frac{40.3}{f^2} \int_{\Delta t} c \cdot N_e dt \end{aligned} \quad (2.6)$$

Let $c \cdot \Delta t = \rho'$ which represents the distance computed by flight time of carrier phase measurements. Now we change the integration variable in the second term to $ds = c dt$, which will change the integration differential dt to transform to the signal propagation differential ds . Thus, we obtain:

$$\rho = \rho' + \frac{40.3}{f^2} \int_s N_e ds \quad (2.7)$$

In Equation (2.7), the second term represents the distance change that the ionosphere has on the carrier phase measurements. It can be spotted that, since the phase velocity is larger than the speed of light in vacuum, the distance derived from the flight time of carrier phase measurements ρ' is shorter than the actual geometric distance ρ .

2.3 Parameterization of Ionospheric Delay

2.3.1 Derivation of Electron Density

The electron density of the ionosphere varies with altitude, as shown in Figure 2.3. As altitude increases, the atmosphere becomes less dense, reducing the number of particles available for ionization, which leads

to a decrease in electron density. However, solar radiation weakens as it passes through the atmosphere. At lower altitudes, where the path is longer, the radiation energy decreases and eventually becomes insufficient to ionize atmospheric particles. The combination of these two factors leads to the variation in ionospheric electron density, which increases with altitude up to a point, and then decreases as altitude continues to rise.

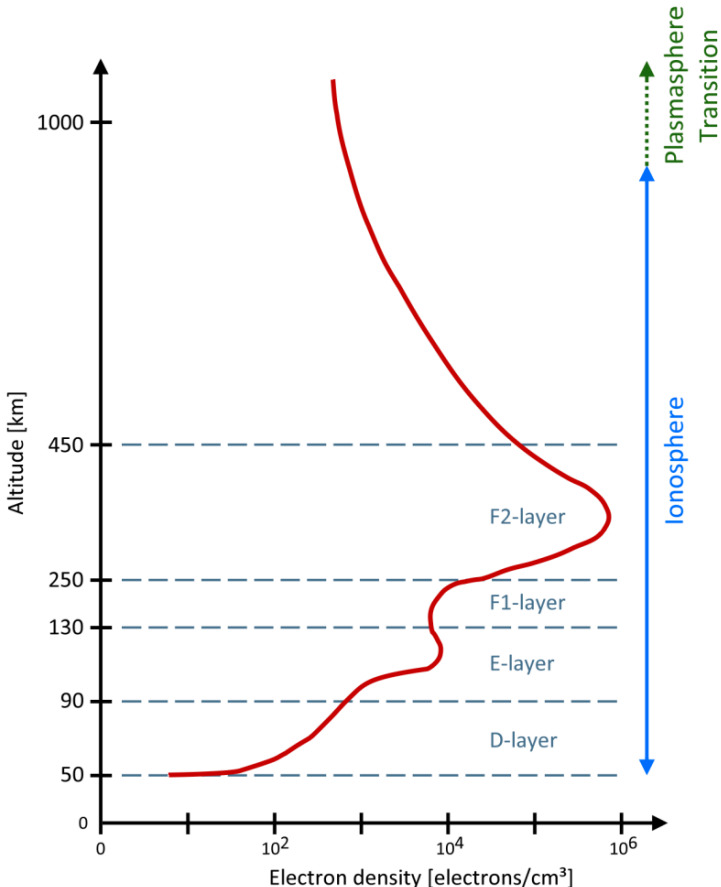


Figure 2.3 Variation of Ionospheric Electron Density with Altitude [21]

Considering that the electron density along the signal propagation path is influenced by both altitude and ionospheric activity, modeling it as a bivariate function can be complex and challenging to represent graphically. Therefore, ionospheric parameterization is commonly performed with the Total Electron Content (TEC).

$$\text{TEC} = \int_s N_e ds \quad (2.8)$$

and Equation (2.7) becomes

$$\rho = \rho' + \frac{40.3}{f^2} \text{TEC} \quad (2.9)$$

Equation (2.9) indicates that TEC is the result of integrating N_e along the propagation path. It can be viewed as the total number of electrons in a column with a unit cross-sectional area extending through the ionospheric path, typically expressed in the unit of total electron content units (TECU) with $1\text{TECU} = 10^{16}\text{electrons/m}^2$.

2.3.2 Mapping Function

After integration, the magnitude of TEC becomes independent of altitude. Based on the elevation angle of the satellite-ground station link, it can be further classified into slant TEC (STEC) and vertical TEC (VTEC). For STEC, a lower elevation angle indicates a longer propagation path through the ionosphere, resulting in a higher TEC value. For VTEC, it is independent of the elevation angle and is solely related to the ionosphere's level of activity. Consequently, VTEC is widely used for ionospheric parameterization and is also a common index used by ionosphere models. Therefore, VTEC is widely used to describe ionospheric activity. Using a mapping function is a simplified method to convert STEC into VTEC. A commonly used model for such conversion is a single layer model (SLM) which assumes that all the electrons are concentrated in a single infinitely thin spherical shell at a certain high altitude [24]. An illustration of the model is shown in Figure 2.4.

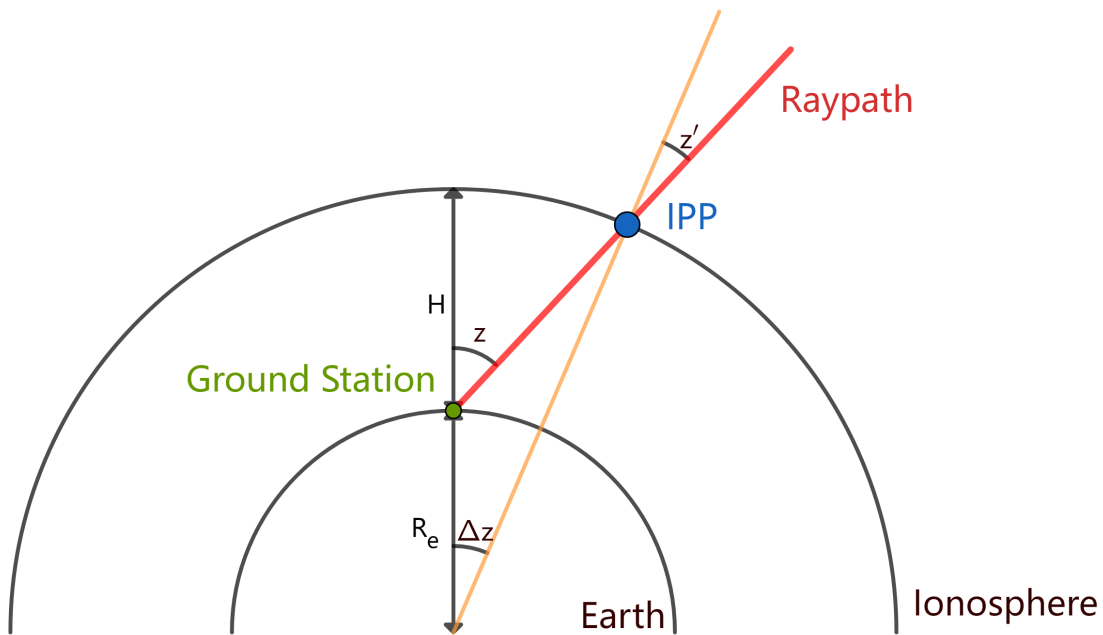


Figure 2.4 Scheme for Ionospheric Single-Layer Model [21]

In Figure 2.4, H is the altitude of the ionospheric single-layer model. R_e represents a mean Earth's radius, z is the zenith angle of the signal path at the measurement station, z' is the zenith angle of the signal path at the ionospheric piercing point (IPP), and $\Delta z = z - z'$ is the angle between the satellite-ground station link vector and the satellite-geocenter link vector.

Among the single-layer models, the modified single-layer model (MSLM) was developed by Center for Orbit Determination in Europe (CODE) and has been widely applied [14]. The mapping process in MSLM is given in Equation (2.10),

$$m(z) = \frac{1}{\cos z'} = \frac{1}{\sqrt{1 - \sin z'^2}} = \left(1 - \left(\frac{R_e}{R_e + H} \sin \alpha z \right)^2 \right)^{-1/2} \quad (2.10)$$

with $\alpha = 0.9782$, single layer height $H = 506.7\text{km}$ and earth radius $R_e = 6371\text{km}$. The conversion from STEC to VTEC using the MSLM can be expressed by the following equation [21]:

$$\text{VTEC}(\text{IPP}(\varphi), \text{IPP}(\lambda), t) = m(z)^{-1} \text{STEC}(x_{gs}, x^s, t) \quad (2.11)$$

The determination of VTEC IPP position can be achieved by the equations below [34]:

$$\begin{aligned} \text{IPP}(\varphi) &= \arcsin (\sin \varphi_{gs} \cos \psi_{ipp} + \cos \varphi_{gs} \sin \psi_{ipp} \cos A) \\ \text{IPP}(\lambda) &= \lambda_{gs} + \arcsin \left(\frac{\sin \psi_{ipp} \sin A}{\cos \varphi} \right) \end{aligned} \quad (2.12)$$

In Equation (2.12), φ and λ represent the latitude and longitude of IPP respectively, φ_{gs} and λ_{gs} represent the latitude and longitude of the ground station, A represents the azimuth angle of the satellite viewed from the ground station, ψ_{ipp} is the geocentric zenith angle given by:

$$\psi_{ipp} = z - \arcsin \left(\frac{R_e}{R_e + H} \sin z \right) \quad (2.13)$$

Equation (2.11) states that if we know the IPP location where the signal passes through the ionosphere and the VTEC value at the point, we can derive the STEC value along the signal propagation path. Conversely, for a known STEC value, the VTEC value at the corresponding IPP position can be derived through a mapping process.

Overall, we can use VTEC from existing ionosphere models to correct the ionospheric delay of signals, and using dual-frequency signals to compute ionospheric delay is a common method for obtaining ionospheric information.

2.4 Existing Ionosphere Models

Currently, there are two types of models used to describe the Vertical Total Electron Content (VTEC) of the ionosphere. One type infers ionospheric activity by describing the Sun's activity, e.g. international reference ionosphere (IRI) [5] while the other directly obtains ionospheric activity through observations of the ionosphere, like global ionospheric maps (GIM).

IRI is the global standard model for the ionosphere, developed jointly by the International Union of Radio Science (URSI) and the Committee on Space Research (COSPAR). Based on decades of satellite, ground-based, and rocket observations, the model utilizes solar indices including the F10.7 index and sunspot number, and provides global distributions of ionospheric parameters such as electron density, temperature, and ion composition. The IRI model can generate global ionospheric parameters for any given date and time, covering data from 1958 to the present, and is widely applied in radio communication, navigation, and academic research.

Notably, the IRI model is an empirical model that predicts various ionospheric parameters based on model inputs. However, With the advancement of satellite communication technology, it has become possible to directly observe the ionosphere using electromagnetic signals, allowing for the development of data-driven models based on actual measurements rather than relying solely on empirical predictions, one of which is GIM.

GIM are global ionospheric models designed to provide high-quality ionospheric information for scientific research and applications. GIM are primarily constructed using dual-frequency GNSS (Global Navigation Satellite System) observation data collected worldwide, allowing them to effectively reflect the dynamic changes and characteristics of the ionosphere. As a model that generates outputs based on real-time data,

GIM features a high temporal resolution for updates. The VTEC products provided by GIM are categorized into rapid solutions with a latency of less than 24 hours, final solutions with a latency of approximately 11 days, and predicted solutions, which are available one and two days in advance². For all three types of VTEC products, the VTEC values are recorded in IONEX (Ionosphere Exchange) format files, which have a spatial resolution of 2.5° (latitude) $\times 5^{\circ}$ (longitude) covering a global extent.

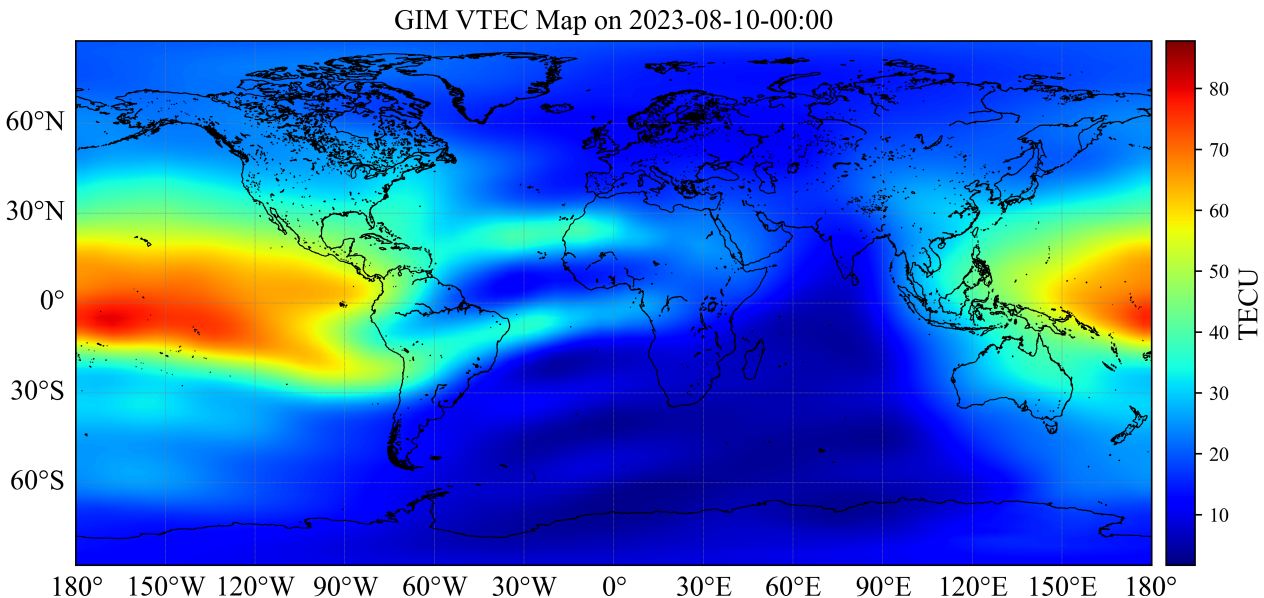


Figure 2.5 Illustration of GIM VTEC Map

2.5 Summary of the Chapter

In this chapter, we discussed the formation of the ionosphere and its impact on electromagnetic signal propagation. The first section introduces the Sun as the primary factor influencing the Earth's ionosphere, explains the source of solar radiation, and presents two indices that reflect solar activity: the sunspot number and the F10.7 index.

The second section of this chapter analyzed the ionospheric delay affecting carrier phase measurements by examining changes in the speed of electromagnetic waves. It concludes that the ionosphere causes the phase velocity of the carrier phase to exceed the speed of light in a vacuum, with this effect being inversely proportional to the square of the signal frequency.

The third section of this chapter introduces methods for quantifying ionospheric delay and explains the conversion between STEC and VTEC using the MSLM model. It also highlights the potential of using dual-frequency signals to observe the ionosphere and retrieve ionospheric information at the corresponding IPP location.

Finally, this chapter introduces two ionospheric models, IRI and GIM, with a particular focus on GIM's temporal and spatial resolution, as well as an overview of the GIM products with different time latencies provided by IGS.

²https://cddis.nasa.gov/Data_and_Derived_Products/GNSS/atmospheric_products.html

3 Satellite Altimetry

Satellite altimetry is designed to measure ground surface elevation and is widely applied in oceanography, hydrology, ice sheet monitoring, and Earth science research. In this chapter, the measurement principle of satellite altimetry, the approach for obtaining ionospheric delays from dual-frequency altimetry observations, and one example of an altimetry satellite, Jason-3, will be introduced.

3.1 Observation Equation of Satellite Altimetry

Carrying radar instruments, the altimetry satellites emit radio waves in the nadir direction and receive the reflected signal from the surface, especially the water surface. The travel time is measured for the calculation of the distance between the satellite and the ground. With known satellite orbit height, the elevation of the ground surface can then be derived. Considering the positive sign of ionospheric delay for ranging signals, the measuring equation of altimetry satellites is:

$$\rho = [P - \Delta_{\text{ION}} + \epsilon]_{f_i} + \epsilon_{\text{ND}} \quad (3.1)$$

In Equation (3.1), P is the measuring range, Δ_{ION} is the ionospheric delay, and ϵ includes other frequency-dependent corrections and measuring noise at frequency f_i [11]. ϵ_{ND} is non-dispersive error including tropospheric delay.

Several different frequencies are used for radar altimeters. The choice depends upon regulations, mission objectives and constraints, technical possibilities – and impossibilities. According to frequency, they can be divided into the following types [3]:

- Ku-band (13.575GHz)

The Ku band is the most commonly used frequency (used for Topex/Poseidon, Jason, Envisat, ERS, etc). It is the best compromise between the capabilities of the technology considering its high frequency, the available bandwidth, and ionospheric perturbation.

- C-band (5.3GHz)

The C band is more responsive to ionospheric disturbances compared to the Ku band while being less affected by atmospheric liquid water. Its primary role is to correct ionospheric delay by forming a combination with the Ku-band.

- S-band (3.2GHz)

The S-band is also used in combination with the Ku-band measurements for the retrieval of the ionospheric delay.

- Ka-band (35GHz)

Signal frequencies in the Ka-band enable better observation of ice, rain, coastal zones, land masses (forests, etc.), and wave heights. Due to international regulations governing the use of electromagnetic wave bandwidth, a larger bandwidth is available than for other frequencies, thus enabling higher

resolution, especially near the coast. It is also better reflected on ice. However, attenuation due to water or water vapor in the troposphere is high, meaning that no measurements are produced when the rain rate is higher than 1.5 mm/h.

The method for retrieving ionospheric delay with dual-frequency altimetry (i.e. Jason-3) is shown below: As can be seen from Equation (3.1), in the measurement equation of altimetry satellites, the ionospheric delay is a frequency-dependent error term. For dual-frequency altimetry satellites, the ionospheric delay can be derived by combining observations with different frequencies. We can form the combination P_{ION} with two range measurements from different frequencies of signals $P_{t,1}^r$ and $P_{t,2}^r$ as:

$$\begin{aligned}
 P_{\text{ION}} &= \frac{f_1^2 f_2^2}{f_1^2 - f_2^2} (P_{t,2}^r - P_{t,1}^r) \\
 &= \frac{f_1^2 f_2^2}{f_1^2 - f_2^2} \left(\frac{40.3}{f_2^2} \text{STEC} - \frac{40.3}{f_1^2} \text{STEC} \right) + \epsilon_{\text{ION}} \\
 &= \frac{f_1^2 f_2^2}{f_1^2 - f_2^2} \left(\frac{f_1^2 - f_2^2}{f_1^2 f_2^2} 40.3 \cdot \text{STEC} \right) + \epsilon_{\text{ION}} \\
 &= 40.3 \cdot \text{STEC} + \epsilon_{\text{ION}}
 \end{aligned} \tag{3.2}$$

Since altimetry satellites always transmit signals in the nadir direction, STEC in the equation can be considered as VTEC. Therefore, the equation to obtain the VTEC at the altimetry IPP using dual-frequency altimetry signals is as follows:

$$\text{VTEC} = 1/40.3 \cdot (P_{\text{ION}} - \epsilon_{\text{ION}}) \tag{3.3}$$

The blue dots in Figure 3.1 show the variation of raw ionosphere measurements calculated using Equation (3.3) over four hours in a day. It can be observed that the VTEC values are highly fluctuating even for quiet ionospheric conditions (20 TECU). To address this, a median filter (represented by the orange curve) is applied to smooth the raw data. For the dual-frequency altimetry measurements used in this study, each original observation is smoothed using a window of 25 surrounding data points.

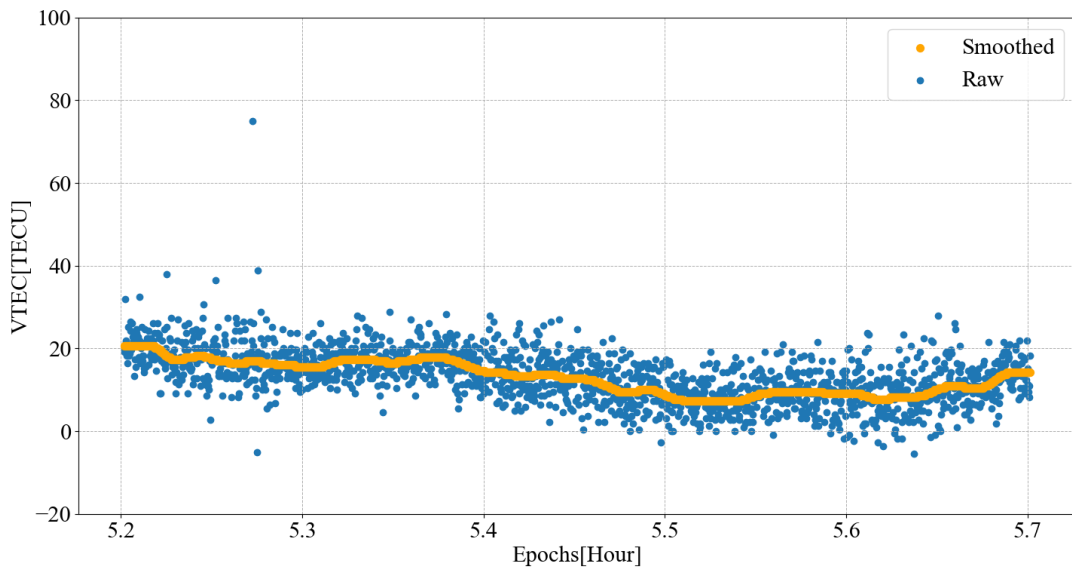


Figure 3.1 Raw and Smoothed Altimetry VTEC

3.2 Altimetry Mission: Introduction of Jason-3

In this thesis, the data used to obtain ionospheric corrections is sourced from Jason-3. This section provides an introduction to the satellite mission.

The Jason-3 mission is an international satellite collaboration aimed at precisely measuring global sea surface height, helping to monitor sea level changes, ocean circulation, and climate patterns. Launched in 2016, the satellite operates in a near-polar orbit at an altitude of approximately 1,336 km with an inclination of 66 degrees, taking around 112 minutes to complete one orbit around the Earth [36]. Jointly conducted by NASA, NOAA, CNES, and EUMETSAT, Jason-3 continues the legacy of the previous Jason satellites, providing data widely used in climate change and ocean dynamics research.

Figure 3.2 shows the variation of DORIS IPP and altimetry IPP positions over one cycle of Jason-3. It can be seen that, thanks to the presence of DORIS ocean-based ground stations and that DORIS operates with dual-frequency signals onboard Jason-3, DORIS can provide ionosphere information within proximity of many altimetry IPP. Consequently, corrections for ionospheric delays at altimetry IPP locations, or DORIS-based altimetry VTEC can be derived from DORIS ionospheric correction data with spatial interpolation. More importantly, since Jason-3's altimetry component also uses dual-frequency signals, the ionospheric corrections obtained directly from altimetry IPP can serve as the ground truth to evaluate the accuracy of DORIS-based altimetry VTEC results.

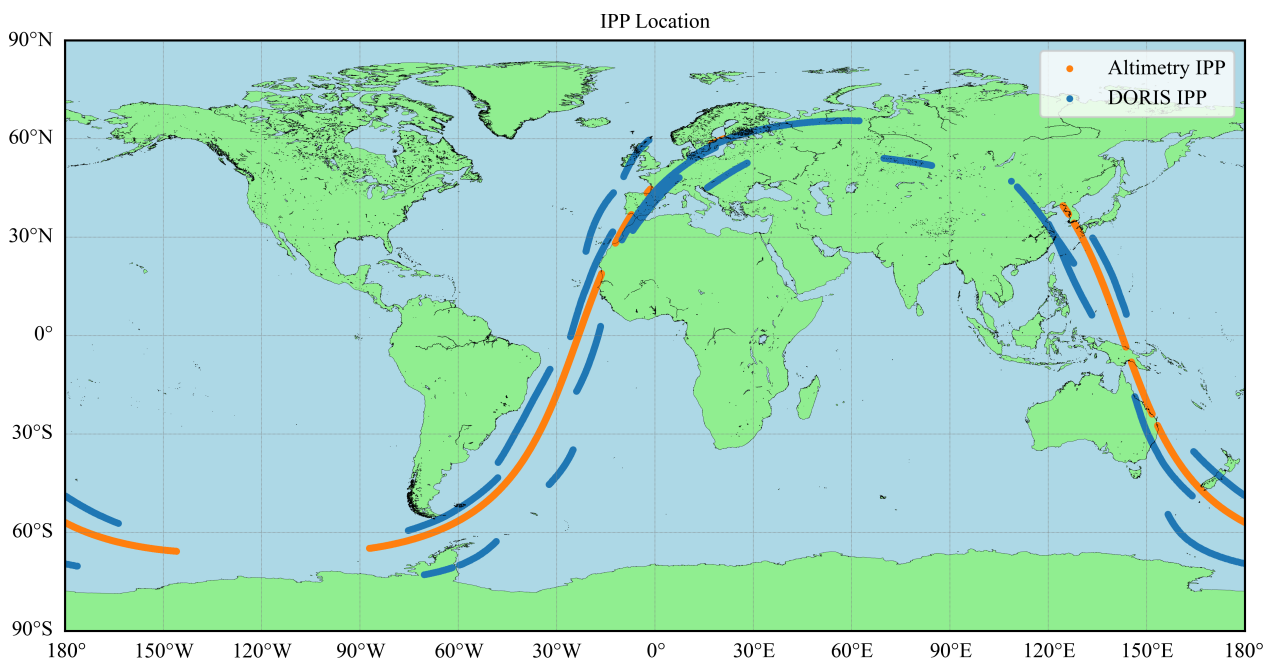


Figure 3.2 IPP Location for Altimetry and DORIS Signals on Jason-3 in one Revolution on 2023 DOY221

3.3 Summary of the Chapter

The first section of the chapter introduced the observation equation for altimetry satellites and the derivation of the equation for obtaining VTEC at the altimetry IPP location using dual-frequency altimetry observations. The temporal instability of altimetry VTEC measurements and the related smoothing method are also discussed in the section.

The second section discusses the Jason-3 mission, highlighting the proximity between DORIS IPP and altimetry IPP locations and emphasizing the potential of using DORIS STEC to provide ionospheric delay information for single-frequency altimetry missions.

4 DORIS

Doppler Orbitography and Radiopositioning Integrated by Satellite (DORIS), is a satellite communication technique widely used in POD for LEO satellites, including altimetry satellites. The DORIS receiver onboard the satellite can obtain precise satellite orbit information by measuring the Doppler shift of signals transmitted from ground stations [31]. This chapter will introduce the basic information regarding the DORIS ground and satellite segments, the observation equation of DORIS measurements, and the method for deriving ionospheric STEC values from DORIS measurements.

4.1 Ground and Satellite Segments

In the DORIS signal transmission system, the reception of DORIS signals and dissemination of observation data are handled by the satellite, while only beacons are required for ground segments to transmit the signals. This low complexity of ground equipment allows DORIS to establish ground stations at various isolated locations around the globe. This characteristic is illustrated in Figure 4.1, where DORIS ground stations are globally distributed, with many located in the oceanic region.



Figure 4.1 2024 Distribution of DORIS Ground Stations. Source: International DORIS Service (IDS), International DORIS Service: <http://ids-doris.org>

Modern DORIS satellites employ DGXX receivers onboard enabling them to track up to seven signals from the ground beacon at a minimum elevation angle of zero [2]. Part of existing satellite missions equipped with DGXX receivers are introduced in Table 4.1.

Table 4.1 Some Altimetry Satellites equipped with DGXX Receiver

| Mission Name | Launch Date | Orbit Type |
|--------------|-------------------|---------------------------|
| Jason-2 | June 20, 2008 | Non-sun-synchronous orbit |
| Jason-3 | January 17, 2016 | Non-sun-synchronous orbit |
| Sentinel-3A | February 16, 2016 | Sun-synchronous orbit |
| Sentinel-3B | April 25, 2018 | Sun-synchronous orbit |

The purposes of these missions indicate a primary focus on oceanic observations. With its ground stations distributed across islands in oceanic regions, DORIS is well-equipped to provide global POD support for these missions. This can be illustrated by Figure 4.2. In the figure, the DORIS IPP are distributed globally, including over oceanic regions, with the colors of the curves indicating the level of ionospheric activity.

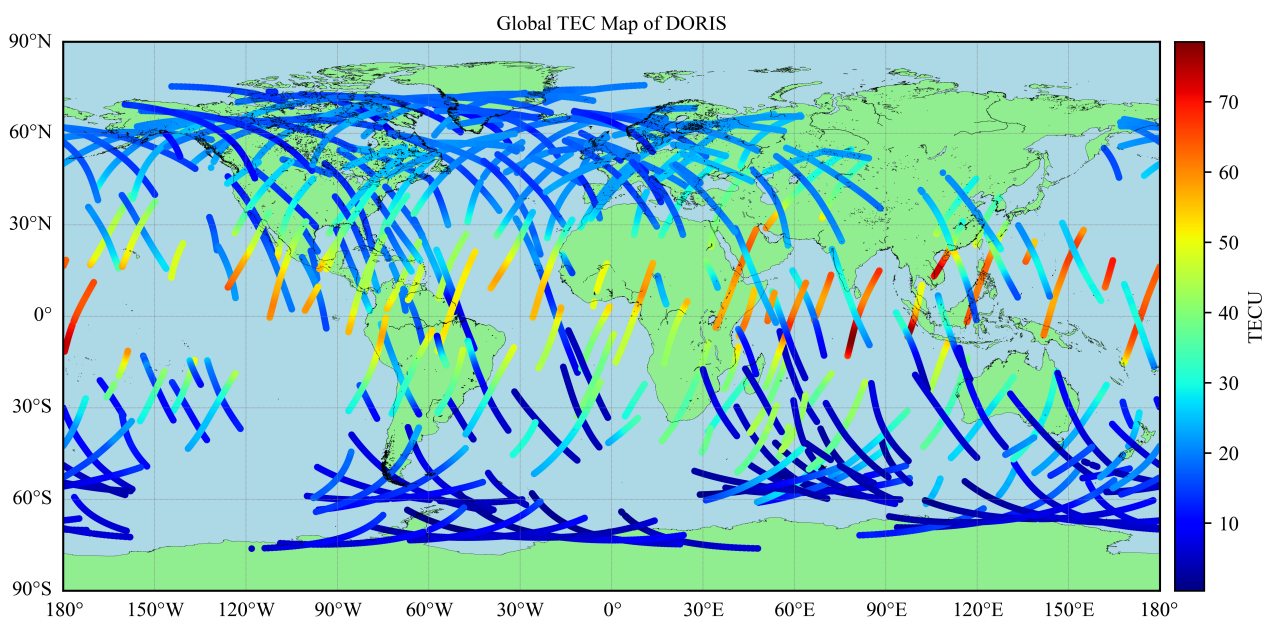


Figure 4.2 Illustration of Jason-3 IPP Location at 2023 DOY 221

4.2 DORIS Data processing

4.2.1 Types of DORIS Observations

Three types of DORIS data are necessary to compute DORIS STEC: ground station coordinates, satellite coordinates, and DORIS measurement data.

- DORIS Ground Station coordinates

The coordinates of the DORIS ground stations are provided by the International DORIS Service (IDS) in the SINEX (Software INdependent EXchange) format¹.

- DORIS Satellite Orbits

The coordinate information for satellite equipped with DORIS can be obtained from IDS, provided in SP3 format².

¹<https://ids-doris.org/>

²ftp://igs.org/pub/data/format/sp3_docu.txt

- DORIS onboard Measurements

The DORIS observations are provided in the RINEX DORIS 3.0 format [23]. This format is derived from the RINEX/GPS format and has been adapted for the phase and pseudo-range measurements of the DGXX instruments³.

4.2.2 Observation Equation of DORIS

Two signals are used in DORIS measurements, with their carrier frequencies of $f_1 = 2,036.25\text{MHz}$ and $f_2 = 401.25\text{MHz}$ in L-band. The pseudo-code is modulated onto two carrier frequencies. Since, DORIS pseudo-code observations have a high noise level, reaching several kilometers [25], making them unsuitable for positioning or ionosphere applications. In comparison, the impact of ionospheric delay is less than one meter. The increased noise in DORIS pseudo-range measurements means the focus of our subsequent discussion will be primarily on carrier phase measurements.

The basic observation equations for carrier phase measurements between the ground station transmitter t and the satellite receiver r are:

$$\Phi_t^r = \rho_t^r + c(\Delta r_t - \Delta r^r) + \Delta_{t,\text{ND}}^r + [-\Delta_{t,\text{ION}}^r + \lambda N]_f + \epsilon_\Phi \quad (4.1)$$

In Equation (4.1), ρ_t^r is the straight line distance between the ground beacon and the satellite, Δr_t and Δr^r are the clock offset, and $\Delta_{t,\text{ND}}^r$ is the combination of all remaining non-dispersive effects. The other terms are in cornered brackets as they are frequency-dependent. As is shown in Equation (2.9), the ionosphere causes the distance measured by phase observations Φ_t^r to appear shorter than the actual distance ρ_t^r , accounting for the negative sign for ionospheric delay term $\Delta_{t,\text{ION}}^r$ in Equation (4.1). N is the carrier phase ambiguity term and refers to the unknown integer number of whole wavelengths between the ground station and the satellite. This term has a constant value for a given pass as long as the data transmission between the station and the satellite is uninterrupted. The final term is the carrier phase noise that could contain multi-path effects and other unmodeled error terms.

4.2.3 Derivation of DORIS STEC

To isolate the ionospheric delay from the above equation and obtain STEC and VTEC values, we need to combine the observations $\Phi_{t,1}^r$ and $\Phi_{t,2}^r$ from two frequencies. Here, we choose a combination that removes the geometric distance and results in the ionospheric delay value. The combination Φ_{ION} is expressed as:

$$\begin{aligned} \Phi_{\text{ION}} &= \frac{f_1^2 f_2^2}{f_1^2 - f_2^2} (\lambda_1 \Phi_{t,1}^r - \lambda_2 \Phi_{t,2}^r) \\ &= \frac{f_1^2 f_2^2}{f_1^2 - f_2^2} \left(\frac{-40.3}{f_1^2} \text{STEC} + \frac{40.3}{f_2^2} \text{STEC} + \lambda_1 N_1 - \lambda_2 N_2 + \Delta D \right) + \epsilon_{\text{ION}} \\ &= \frac{f_1^2 f_2^2}{f_1^2 - f_2^2} \left(\frac{f_1^2 - f_2^2}{f_1^2 f_2^2} 40.3 \cdot \text{STEC} + \lambda_1 N_1 - \lambda_2 N_2 + \Delta D \right) + \epsilon_{\text{ION}} \\ &= 40.3 \cdot \text{STEC} + \frac{f_1^2 f_2^2}{f_1^2 - f_2^2} (\lambda_1 N_1 - \lambda_2 N_2 + \Delta D) + \epsilon_{\text{ION}} \end{aligned} \quad (4.2)$$

this yields

$$\text{STEC} = 1/40.3 \cdot (\Phi_{\text{ION}} - \frac{f_1^2 f_2^2}{f_1^2 - f_2^2} (\lambda_1 N_1 - \lambda_2 N_2 + \Delta D) + \epsilon_{\text{ION}}) \quad (4.3)$$

³<ftp://ftp.ids-doris.org/pub/ids/data/IntroductionToDORISRINEX.pdf>

In Equation (4.3), the integer ambiguity remains a frequency-dependent term that has not been separated. To solve this issue a leveling process is required, and the method will be introduced in Chapter 5. Additionally, when considering the difference between observations at two different frequencies, the antenna phase center offset must be accounted for as a significant source of error. A demonstration of phase center error is illustrated in Figure 4.3.

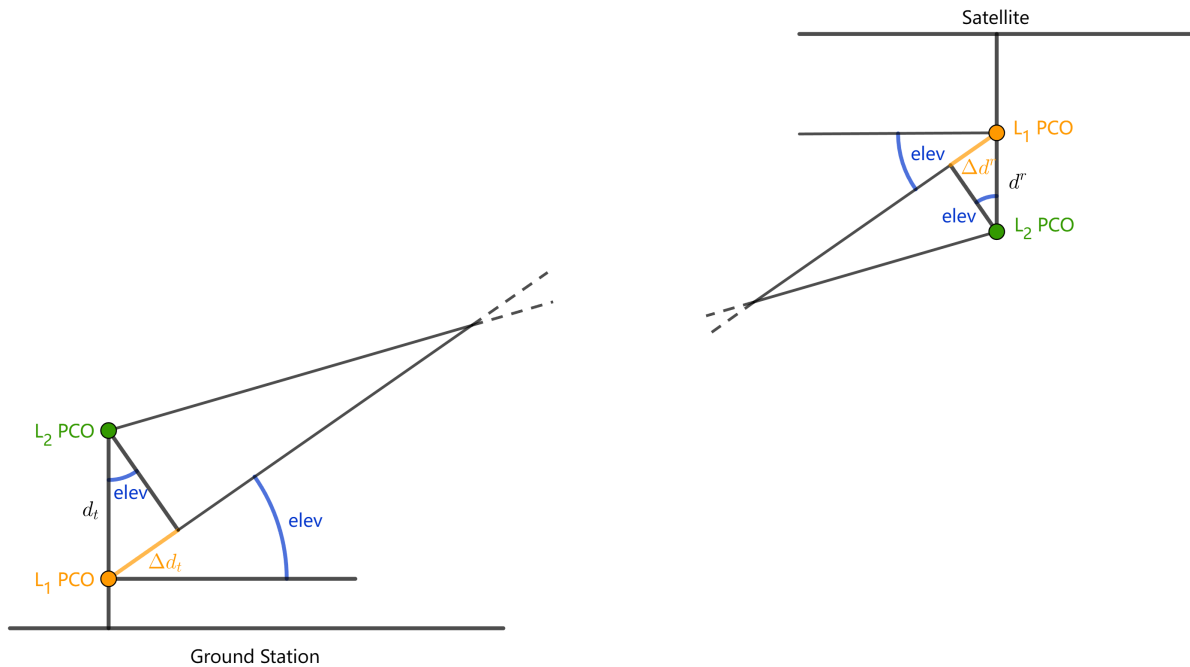


Figure 4.3 Illustration of Phase Center Error [21]

In Figure 4.3, the actual differences in Phase Center Offsets (PCO) between the two frequencies at the ground segment and the satellite segment are zenith offset d_t and nadir offset d^r , respectively. The distance projected in the link direction can be expressed as:

$$\Delta D = \Delta d_t + \Delta d^r = (d_t + d^r) \sin(elev) \quad (4.4)$$

where $elev$ is the elevation of the satellite.

Different satellites and various types of antennas of ground stations have distinct values for d_t and d^r . Table 4.2 shows the specific values for DORIS satellites currently in orbit, as well as two types of antennas used at operational ground stations.

Table 4.2 Offsets for Satellites and Ground Beacons

| Type | Mission | Offset [m] |
|-----------|---------|------------|
| Beacon | Alcatel | 0.175 |
| | STAREC | 0.487 |
| Satellite | Jason-2 | 0.164 |
| | Jason-3 | 0.168 |

Some factors are not considered in Equation (4.3):

- Higher Order Ionospheric Delay Term

As is discussed in the second chapter, the magnitude of ionospheric delay is inversely proportional to the square of the signal frequency and directly proportional to the activity level of the Earth's magnetic field. For lower-frequency f_2 DORIS signals, higher-order ionospheric delay terms can affect the geometric distance by up to 60 cm [26].

- Phase Wind-Up Effect

In this thesis, phase variations resulting from the phase wind-up effect (PWU) are not considered. The PWU arises from the satellite's continuous rotation to orient its solar panels towards the sun, and it is affected by the relative positioning of the transmitter and receiver antennas, along with the direction of the line of sight. The maximum influence of PWU on the Jason-2 satellite can achieve 30 cm for an inverted satellite orientation [26]. While the impact of PWU is much smaller for most conditions, this should be noted as one source of error that could reach a decimeter level.

- Differential Phase Bias

The Differential Phase Bias (DPB) arises from the difference in hardware channel delays when transmitting different carrier phase signals. For GNSS signals, this bias can be several tens of nanoseconds or several meters, making it a critical error source that must be considered for precise GNSS positioning. However, DCB is directly related to hardware and remains stable over long periods. Therefore, for DORIS observation combinations, this bias, along with the ambiguity term, will be eliminated after the leveling process (introduced in the next chapter).

- DORIS Frequency Shift

The transmitted frequencies of 3rd and 4th generation DORIS beacons may be shifted with respect to the nominal DORIS frequencies to avoid jamming with other beacon in the vicinity. This function is used only when two channels or more are available on the satellite DORIS instrument that is to say with the 2G, 2GM and DGXX receivers⁴. For a signal with $f_2 = 401.25\text{MHz}$, the maximum frequency shift can reach 12.5kHz. The impact of such a frequency shift on ionospheric delay calculations corresponds to an order of magnitude of 0.001% for the ionospheric delay, which is smaller than the effect caused by neglecting higher-order ionospheric delays.

4.3 Summary of the Chapter

This chapter introduces the DORIS system, with the first section focusing on its satellite and ground segments. DORIS operates with ground equipment, using beacons distributed across various locations worldwide, including many in oceanic areas. These beacons send signals to satellites equipped with DORIS receivers, which track the signals to determine the satellite's precise orbit. This satellite-based system is widely applied in missions regarding oceanic and Earth observations, as seen in missions like Jason-3 and Sentinel-3A.

The second section outlines the DORIS observation equation and thus outlines the method to attain STEC. Three primary types of data are needed for STEC derivation: the coordinates of ground stations, satellite orbits, and the DORIS measurements. Next, the observation equation for DORIS carrier phase measurements is introduced, which accounts for geometric distances, clock offsets, non-dispersive effects, ionospheric delays, and phase ambiguities. Moreover, the method for deriving STEC from dual-frequency DORIS measurements is explained. By combining phase measurements at two frequencies, the geometric distance is eliminated, allowing for the calculation of ionospheric delay. However, some error sources,

⁴[ftp://ftp.ids-doris.org/pub/ids/stations/Interface_Specification_Between_Beacons_And_Onboard_Instrument.pdf](http://ftp.ids-doris.org/pub/ids/stations/Interface_Specification_Between_Beacons_And_Onboard_Instrument.pdf)

including differential phase bias and carrier phase ambiguity, cannot be solely eliminated through DORIS observations, and the relevant methods will be introduced in Chapter 5.

5 Methods: From DORIS STEC to DORIS-based Altimetry VTEC

In the fourth chapter, the method for calculating STEC from DORIS dual-frequency carrier phase observations was introduced. However, due to the lack of pseudo-range measurements, the computed STEC lacks an absolute reference, requiring assistance from other observation methods to obtain accurate ionospheric information. This chapter will introduce a leveling method for correction. Additionally, in the third chapter, we discussed the potential for calculating altimetry VTEC through interpolation of DORIS VTEC. Therefore, this chapter will also introduce possible interpolation methods and the related data selection strategies to obtain DORIS-based altimetry VTEC from DORIS VTEC measurements.

5.1 DORIS STEC Leveling

Due to increased noise, the pseudo-range from DORIS cannot be utilized for carrier smoothing or code leveling. As mentioned in Section 4.2, the missing level in DORIS data is caused by the unresolved ambiguity of the integer cycles, which are assumed to remain constant throughout a complete pass. Therefore, we can use other ionospheric models to provide a reference for each DORIS pass, and the method for DORIS leveling has been extensively described by Dettmering et. al [7]. In this study, we use GIM as the VTEC source for this leveling process. The model used here is provided by the International GNSS Service (IGS) and represents a global ionospheric model that combines results from seven data analysis centers.

Since the integer cycle ambiguity is assumed to remain constant only within a complete pass, the leveling of DORIS STEC is performed on a per-pass basis. Among all the observations in a single pass, the observation with the highest elevation angle is used to establish the reference. This approach is chosen because a large elevation angle reduces errors from the mapping function and minimizes path-dependent errors due to the shorter propagation distance. With the selected point, we can further compute the delta value for GIM and DORIS STEC, which is then applied to the entire pass. A demonstration of the whole process is shown in figure 5.1.

Although the leveling process is not complex, to obtain DORIS VTEC using GIM and DORIS STEC, the following steps are required [7]:

- Pass Detection

For a series of observations generated between a DORIS satellite and any ground station, it is necessary to filter out outliers or interrupted observations to ensure that the observations within a pass share the same integer cycle ambiguity. Here, we assume that two consecutive uninterrupted observations should exhibit similar ionospheric delay values, or $|\Phi_{\text{ION},t} - \Phi_{\text{ION},t-1}| < 0.2\text{m}$.

Moreover, each pass must meet the following three conditions: the time interval between consecutive observations should be less than 60 seconds, each observation value must lie within 3 standard deviations of the observation mean value of the pass, and each pass must contain at least 50 observations. Overall, this processing will eliminate approximately 10% of observed DORIS data.

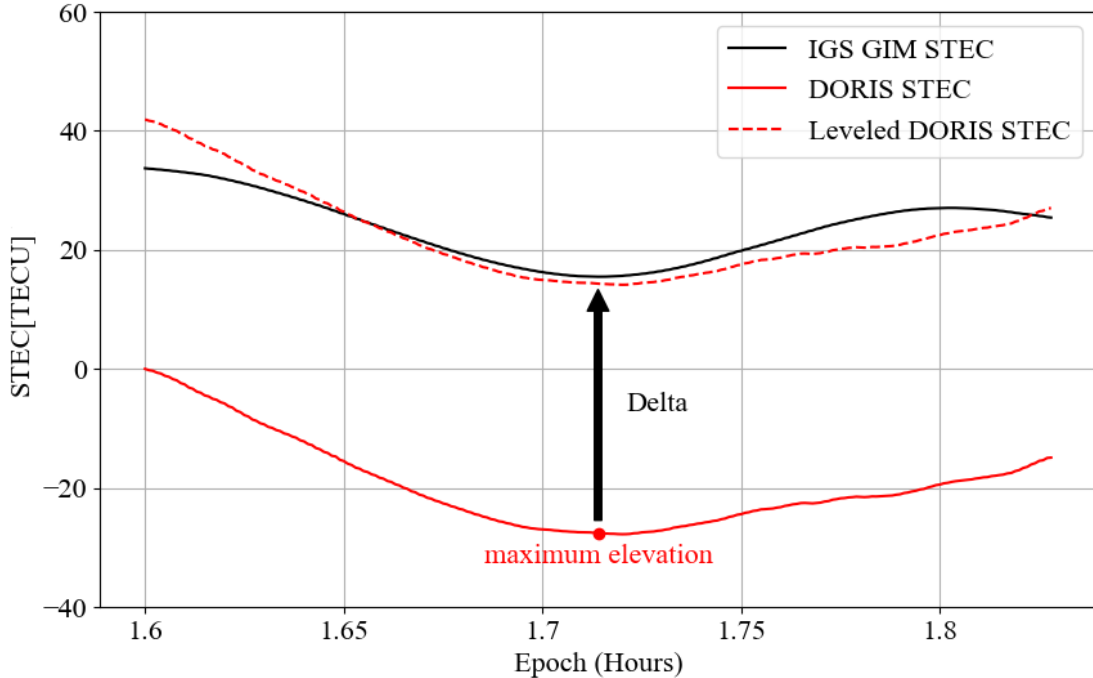


Figure 5.1 Illustration of STEC Leveling

- GIM VTEC Interpolation

Since the recording time and spatial interval of DORIS STEC are continuously varying, the GIM data must be subjected to spatial and temporal interpolation before it can be used for leveling reference.

The interpolation method is given by Equation (5.1). Linear interpolation is employed for the temporal dimension, while bilinear interpolation is used in the latitude and longitude grid to obtain the TEC values at any arbitrary time and spatial point [12].

$$\begin{aligned}
 \text{VTEC}(\varphi_i + q \cdot \Delta\Phi, \lambda_k + p \cdot \Delta\Lambda, t) \\
 = (1 - q) \cdot (1 - p) \cdot \text{VTEC}(\varphi_i, \lambda_k, t) \\
 + q \cdot (1 - p) \cdot \text{VTEC}(\varphi_i + \Delta\Phi, \lambda_k, t) \\
 + p \cdot (1 - q) \cdot \text{VTEC}(\varphi_i, \lambda_k + \Delta\Lambda, t) \\
 + q \cdot p \cdot \text{VTEC}(\varphi_i + \Delta\Phi, \lambda_k + \Delta\Lambda, t)
 \end{aligned} \tag{5.1}$$

In the GIM grid, (φ_i, λ_k) is the grid point whose latitude and longitude are both smaller than those of the DORIS IPP point and are the closest to it. $\Delta\Phi = 2.5^\circ$ and $\Delta\Lambda = 5^\circ$ are the grid intervals of GIM, with $0 \leq q \leq 1$ and $0 \leq p \leq 1$ expressing the percentage position of the DORIS IPP within the latitude and longitude grid.

- GIM VTEC Scaling

For any satellite communication method, the geometric conditions of observation limit the signal to only traverse the portion of the ionosphere below the satellite. The GNSS satellites used for the reference GIM operate at altitudes exceeding 20,000 km, allowing them to cover all components of the ionosphere. In contrast, the DORIS signals used in LEO satellites can only penetrate a certain proportion of the ionosphere. A height-dependent scaling factor with

$$\text{VTEC}_{\text{DORIS_height}} = \text{ScalingFactor} \cdot \text{VTEC}_{\text{GIM_height}} \tag{5.2}$$

should be deployed to correct this effect [32], as Table 5.1 shows.

Table 5.1 Scaling Factor for Some Altimetry Missions

| Mission | Orbit Height [km] | Scaling Factor |
|---------|-------------------|----------------|
| Jason-3 | 1350 | 0.925 |
| HY-2A | 970 | 0.880 |
| SARAL | 800 | 0.856 |

After interpolation and scaling, we can obtain GIM VTEC data at the position of the DORIS IPP covering the range from the ground to the DORIS satellite orbit height.

- Mapping Function

In the leveling process illustrated in Figure 5.1, STEC from the IGS GIM is used as the reference level. Therefore, it is necessary to map the GIM VTEC to the STEC value using DORIS elevation at the corresponding IPP position, with the mapping function introduced by Equation (2.10). It is not recommended to first map DORIS STEC to DORIS VTEC and then compare DORIS VTEC with GIM VTEC, as the uncorrected DORIS STEC contains cycle ambiguities that are not related to the elevation angle, which introduces additional errors in the mapping process.

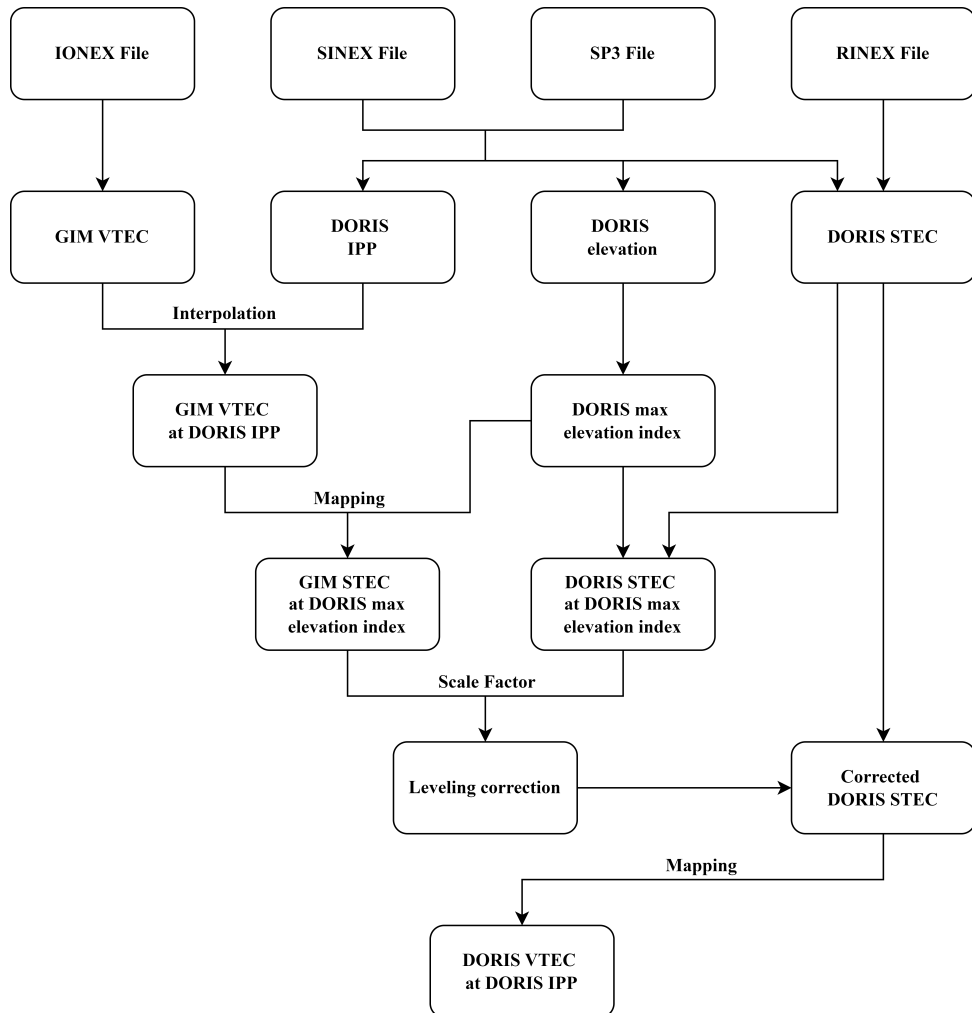


Figure 5.2 Computation Flow of STEC Leveling

The flow chart 5.2 illustrates the whole process of combining DORIS STEC and IGS VTEC to obtain DORIS VTEC. The first row of the flow chart is at the data input level, while from the second row onward, the process is done for each pass, with the output being the DORIS VTEC values of the pass.

5.2 DORIS-based Altimetry VTEC Derivation from DORIS VTEC

From Figure 3.2, it can be seen that there are many DORIS IPP passes near the altimetry IPP track. Each segment of the DORIS IPP track is generated by the signal transmission between the satellite and a specific DORIS ground station. Since DORIS ground stations are distributed across global oceanic regions, most of the altimetry IPP locations are covered by at least one DORIS IPP pass.

In the previous section, we established a method for correcting DORIS STEC to DORIS VTEC with GIM VTEC as a reference. Since this thesis aims to provide TEC support for single-frequency altimetry satellites equipped with the DORIS system, this section introduces the approach for obtaining DORIS-based altimetry VTEC using DORIS VTEC. This includes various parameters for data selection and different interpolation methods. First, appropriate criteria should be applied to select DORIS IPPs and their VTEC values for each altimetry IPP. Second, we can use these DORIS VTEC values to perform interpolation and obtain DORIS-based altimetry VTEC at the altimetry IPP.

5.2.1 Data Preprocessing

For a given altimetry IPP location, there are two methods for data selection: one based on time intervals and the other based on spatial region boundaries.

- Time Division

For time division, only those DORIS observations taken in a given time interval within the altimetry observation epoch will be selected. Considering the low orbit height of Jason-3 (as shown in Table 5.1), the DORIS IPP locations will only form a small distance from the altimetry IPP. This proximity allows the DORIS IPP to reflect the ionospheric activity near the altimetry IPP location.

The parameter introduced using this division approach is the time interval near the observation time of the altimetry IPP. Additionally, a minimum number of DORIS IPP observations within this time window should be necessary, since if too few DORIS observations are selected, their representation of the ionospheric delay at the altimetry IPP location will be poor. Another data quality filtering criterion that can be used is the elevation angle. Setting a minimum elevation mask helps avoid data with large errors from contaminating the data quality of the interpolation points.

- Spatial Division

In spatial division, we select DORIS IPPs within a specific spatial region near the altimetry IPP for subsequent interpolation processes. The parameters introduced by the spatial division method include the spatial range around the altimetry IPP, the number of DORIS observation points within this range, as well as the elevation mask.

An illustration of the strategy is shown in Figure 5.3. In the figure, for the blue altimetry IPP, only the red DORIS IPPs within the black rectangle will be selected for the next interpolation step.

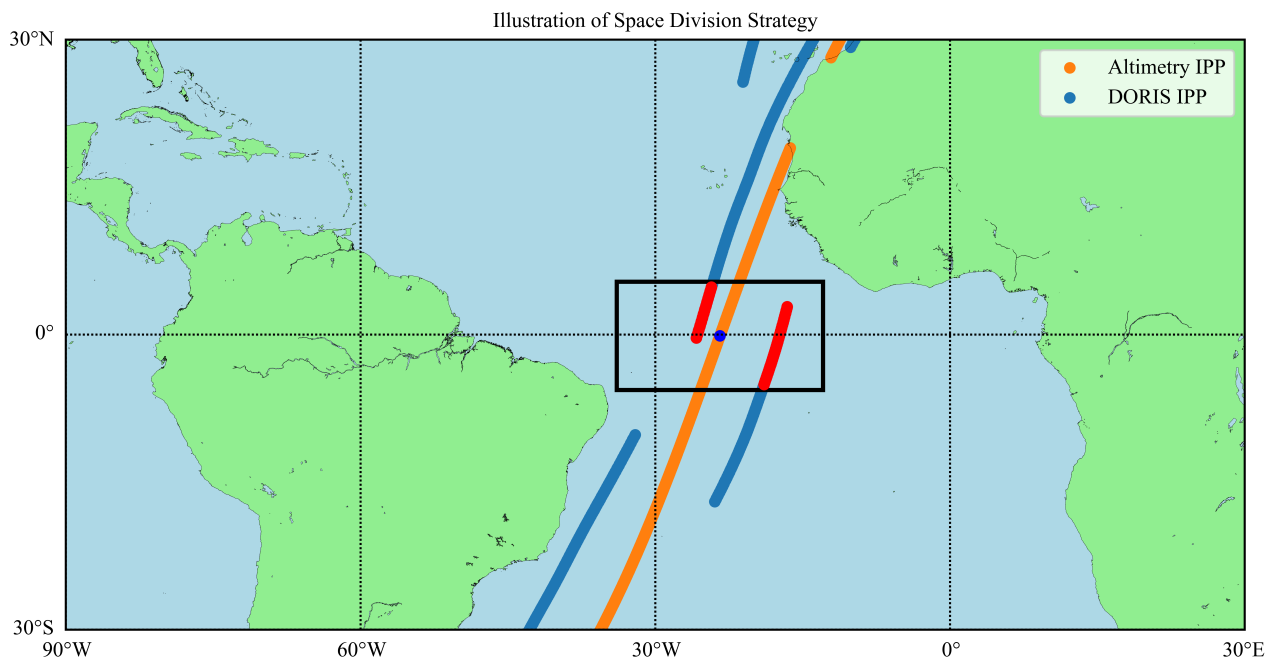


Figure 5.3 Illustration of Space Division Strategy

After the selection of DORIS IPP within the appropriate region, an outlier test must be conducted to remove anomalous VTEC values that lie beyond three standard deviations from the mean. This step helps reduce the likelihood of using unreliable data in the subsequent interpolation.

Moreover, since the observation time of the selected DORIS IPP does not coincide with the observation time of the altimetry IPP VTEC (with a maximum time difference of approximately two minutes), we also need to account for ionospheric variations arising from this time difference. This variation can be described by the Earth's relative motion with respect to the Sun. Due to the Earth's rotation from west to east, the ionospheric conditions at a certain IPP and time should correspond to the conditions at an earlier time at a location further east, assuming no significant changes in solar activity. To correct this effect, we should use the observation time of the altimetry IPP as the reference. IPP points observed by DORIS at earlier times should be shifted eastward, while those observed at later times should be shifted westward. The shift magnitude corresponds to a full rotation of 360° in 24 hours.

In this thesis, time correction is not performed by interpolation for two main reasons: First, there are not many DORIS IPP points near each altimetry IPP, and the observation times of these IPPs change continuously, leaving insufficient points for time-domain interpolation. Second, within such short time intervals of different DORIS observations (no more than 5 minutes), solar activity remains relatively stable, and the primary cause of VTEC variation in the ionosphere is the Earth's rotation.

5.2.2 Data Interpolation

Two interpolation methods are tested in the thesis: Inverse Distance Weighting (IDW) and Kriging interpolation.

- Inverse Distance Weighting Interpolation

The principle behind IDW is that the closer (in space or time) a known point is to the unknown point, the more influence (or weight) it has in the estimation. Conversely, points more far away have less influence. The weight for a point i with distance to the target point of d_i is

$$w_i = \frac{1}{d_i^p} \quad (5.3)$$

where p is a power parameter that controls how quickly the weight decreases with distance. In the thesis, this parameter is set to 2. The estimated value \hat{z}_o at the unknown point is calculated using the weighted average of the known values:

$$\hat{z}_o = \frac{\sum_{i=1}^n w_i z_i}{\sum_{i=1}^n w_i} \quad (5.4)$$

- Kriging Interpolation

Kriging interpolation is a geostatistical technique used to estimate unknown values at unsampled locations based on known data points [28]. Kriging interpolation follows the first law of geography, which posits that spatially close attributes are more similar than those further apart, and it employs the spatial distance relationship to characterize the correlation between attributes. In this interpolation method, the attribute value to be estimated at the point o is also given by:

$$\hat{z}_o = \sum_{i=1}^n w_i z_i \quad (5.5)$$

Unlike IDW, the weight of the known points is not purely dependent on distance but also related to the attribute similarities for these points as:

$$\begin{bmatrix} r_{11} & r_{12} & \cdots & r_{1n} & 1 \\ r_{21} & r_{22} & \cdots & r_{2n} & 1 \\ \cdots & \cdots & \cdots & \cdots & \cdots \\ r_{n1} & r_{n2} & \cdots & r_{nn} & 1 \\ 1 & 1 & \cdots & 1 & 0 \end{bmatrix} \begin{bmatrix} w_1 \\ w_2 \\ \cdots \\ w_n \\ -\phi \end{bmatrix} = \begin{bmatrix} r_{1o} \\ r_{2o} \\ \cdots \\ r_{no} \\ 1 \end{bmatrix} \quad (5.6)$$

In the matrix, ϕ is the Lagrange multiplier, ensuring that the estimation of the target point is unbiased, i.e., $\sum_{i=1}^n w_i = 1$. The attribute similarities of the points are described by the variogram function r_{ij} , where

$$r_{ij} = \frac{1}{2} E [(z_i - z_j)^2] \quad (5.7)$$

z_i and z_j are the attribute values at points (x_i, y_i) and (x_j, y_j) . The function value of the variogram can only be acquired when the attribute values of both points are known, which means on the right side of Equation 5.6 where one of the pair is point o , the function values are to be determined.

According to the first law of geography, the magnitude of spatial distance can be used to describe the values of the variogram function expressed as $r = r(d)$, with distance d_{ij} in

$$d_{ij} = d(z_i, z_j) = d((x_i, y_i), (x_j, y_j)) = \sqrt{(x_i - x_j)^2 + (y_i - y_j)^2} \quad (5.8)$$

To establish this relationship between r and d , we first need to calculate the distance d_{ij} between each pair of known points and the corresponding variogram function value r_{ij} . We then employ a fitting function to derive the specific form of $r(d)$, and finally this can be used to establish the relationship between $d_{1o}, d_{2o}, \dots, d_{no}$ (known distance) and $r_{1o}, r_{2o}, \dots, r_{no}$ (unknown variogram function value). In this manner, all values in the matrix are known, allowing us to calculate the weight values.

In this paper, a linear fitting model is applied, with the following form:

$$r(d) = C_0 + C_1 d$$

Where: $r(d)$ is the variogram value at a given distance d , C_0 is the nugget effect (base variogram), C_1 is the slope of the linear increase and d is the spatial distance between two points.

Using the preprocessed DORIS VTEC data and applying the two interpolation methods mentioned above, we can finally obtain DORIS-based altimetry VTEC, which could be used to correct ionospheric delay for single-frequency altimetry observations.

5.3 Summary of the Chapter

This chapter presents the methods for deriving altimetry VTEC from DORIS STEC. First, the process of DORIS STEC leveling is introduced. As DORIS lacks pseudo-range measurements, a leveling procedure is necessary to correct for integer cycle ambiguity. The ionospheric product applied in this thesis is GIM from IGS in this thesis. The leveling process is performed on a per-pass basis, where the observation with the highest elevation angle is used to establish the reference.

Next, the methodology for derivation of DORIS-based altimetry VTEC from DORIS VTEC is explained. The preprocessing part focuses on selecting DORIS IPPs near the altimetry IPP track. Criteria based on time intervals and spatial proximity are used to select appropriate DORIS measurements, with time corrections applied to account for the Earth's rotation. Following data selection, the chapter covers the interpolation methods used to estimate altimetry VTEC. Two interpolation techniques — IDW and Kriging are employed. IDW uses spatial proximity to weigh the observations, while Kriging incorporates spatial correlation to estimate ionospheric conditions at the altimetry IPP locations. After preprocessing and interpolation, DORIS-based altimetry VTEC can finally be derived.

Overall, this chapter follows Chapter 4 and describes the process of converting unleveled DORIS STEC into DORIS-based altimetry VTEC, which can be used for ionospheric correction in single-frequency altimetry.

6 Results and Analysis

Using the methodology introduced in the previous chapter, this chapter presents the TEC results obtained from the DORIS system and conducts analysis and comparisons based on these results. Specifically, the content is divided into four sections. First, the impact of different local time and ionospheric activities on the leveling results during the STEC leveling process is analyzed. Next, this chapter examines the effect of different parameter combinations selected for DORIS VTEC interpolation in generating DORIS-based altimetry VTEC. Following the parameter selection, a comparison of two interpolation methods (Inverse Distance Weighting and Kriging Interpolation) will be conducted. Finally, based on the optimal parameter combinations and interpolation method identified through discussion, a comparison between DORIS-based altimetry VTEC and GIM-based altimetry VTEC at Altimetry IPP will be carried out, in which the accuracy and data coverage percentage will be illustrated. For the comparison, 30 days of data from November and December 2019 were analyzed to assess DORIS corrections under quiet conditions, while 30 days of data from May to June 2024 were used to evaluate DORIS corrections during active conditions, aiming to achieve results that perform well under varying ionospheric activity levels.

6.1 DORIS STEC: Leveling

The STEC leveling method was introduced in Section 5.1. Here, the relation between local time and STEC values in different ionospheric periods is shown in Figure 6.1 and 6.2.

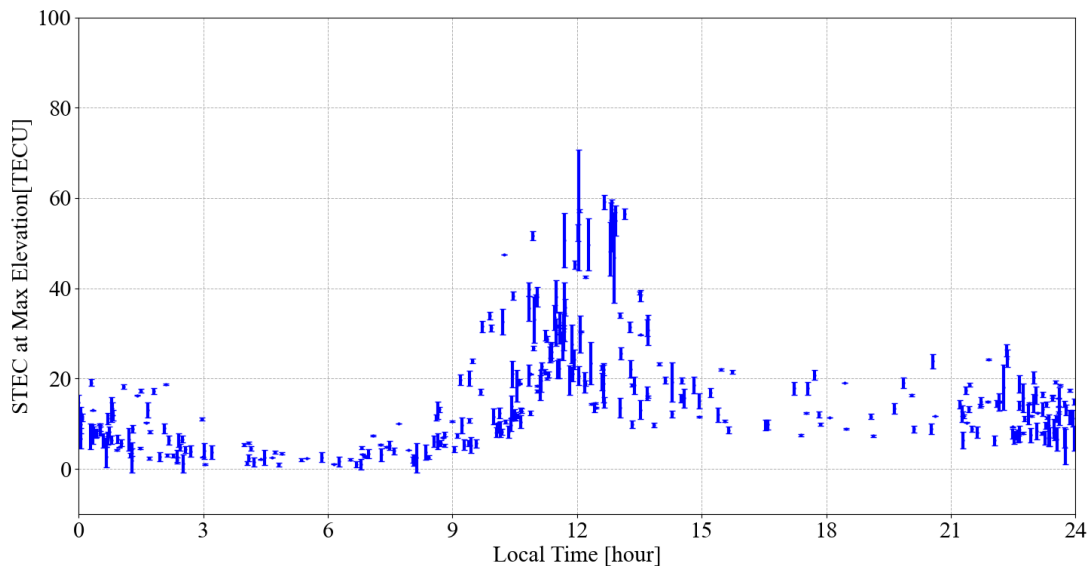


Figure 6.1 Relation between STEC and Local Time on 2019 DOY334 (Quiet)

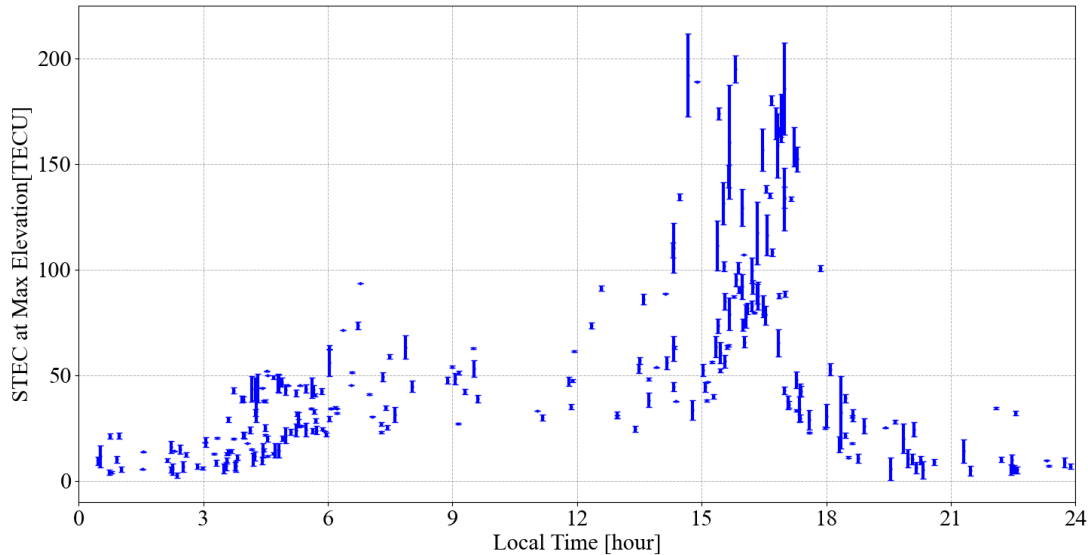


Figure 6.2 Relation between STEC and Local Time on 2024 DOY129 (Active)

In Figure 6.1 and 6.2, each bar represents one DORIS pass within the day and the related GIM STEC value at the max elevation point. The length of the bar indicates the RMS value of the difference between the DORIS STEC and the GIM STEC for the pass. Since the leveling process selects the point with the highest elevation angle in each pass for the computation of delta (Figure 5.1), the corresponding STEC value at the point will also be chosen to represent the ionospheric activity throughout the pass. As can be observed from both figures, those passes with higher absolute STEC values exhibit larger RMS values (longer bar length), indicating a larger discrepancy compared to the GIM results.

The average RMS values for all passes, and related average GIM STEC values throughout the day, are listed below:

Table 6.1 Average RMS values in Leveling for Quiet and Active Conditions

| | Quiet Condition 2019 DOY 334 | Active Condition 2024 DOY 129 |
|-----------------------|---------------------------------|----------------------------------|
| GIM STEC [TECU] | 15.3 | 49.3 |
| RMS(GIM-DORIS) [TECU] | 1.26 | 3.23 |

In the more active ionospheric conditions illustrated in the 6.2, the overall average RMS value is notably larger than those in quiet conditions, exceeding 3 TECU. However, it is also important to note that TEC results from the GIM may not fully capture actual ionospheric activity, meaning that a large RMS value does not necessarily reflect low-quality observational results for DORIS (and vice versa).

From the perspective of local time, we observe that the peaks of STEC (or error bars) on different DOYs occur at different local times. This variation arises from the fact that Jason-3 operates in a sun-synchronous orbit, meaning that its local crossing time over a given location differs in each revolution. To describe the change in the local time of the ascending node (LTAN), the magnitude is approximately -2.0 hours per 10 days.

The relation between local time and IPP latitude for these two days is illustrated in Figure 6.3. For DOY 334 in 2019, at approximately 00:00 and 12:00 local time Jason-3 crosses the equator, where the ionosphere

is most active (as can be seen from Figure 2.5). Since the local regions are not exposed to sunlight at 00:00, it is reasonable that the STEC peak appears at 12:00 local time in Figure 6.1.

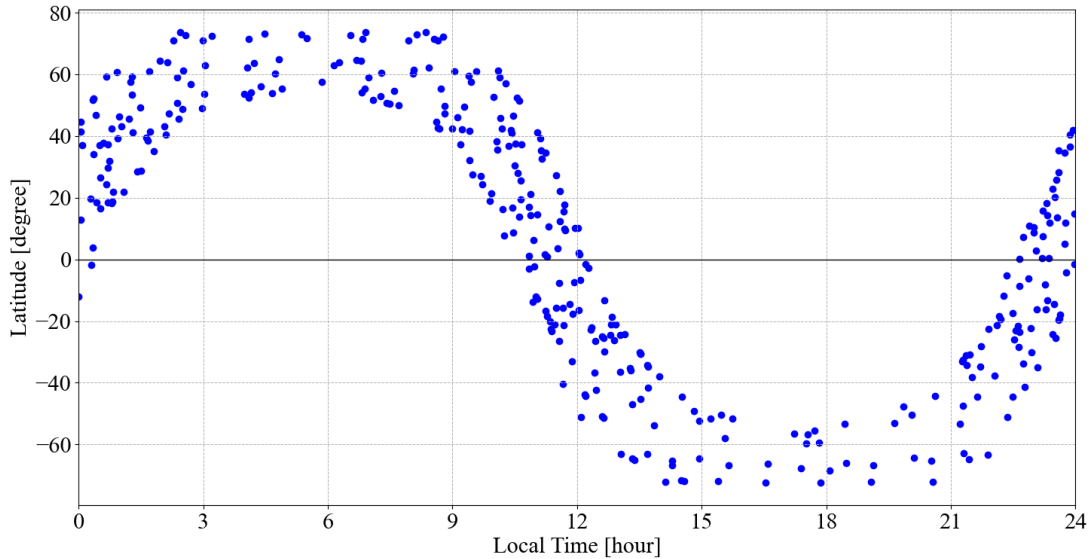


Figure 6.3 IPP Latitude at 2019 DOY 334 (Quiet)

A similar phenomenon can be observed in the comparison between Figure 6.4 and 6.2, where Jason-3 crosses the equator around 16:00 local time.

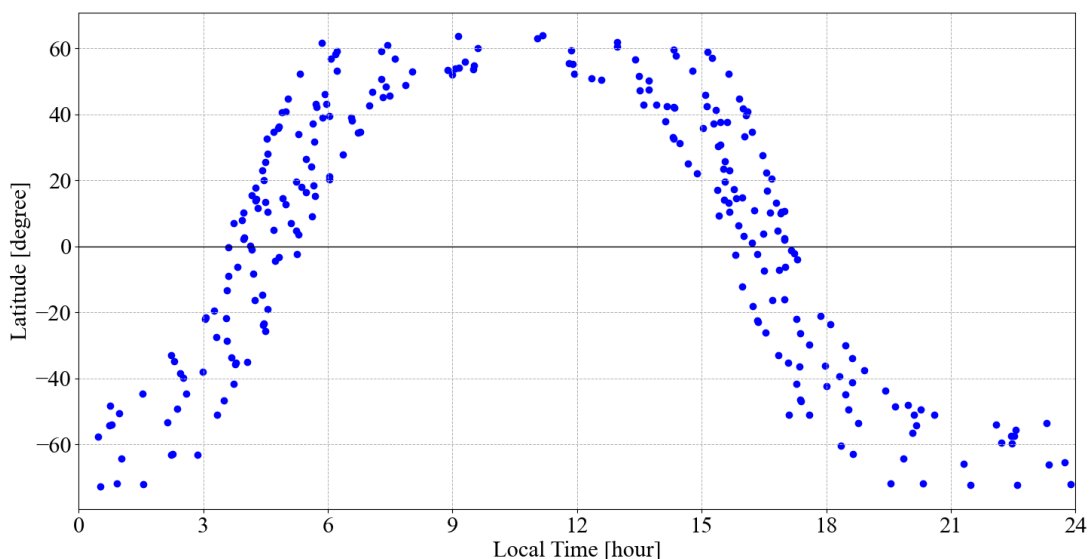


Figure 6.4 IPP Latitude at 2024 DOY 129 (Active)

6.2 DORIS-based Altimetry VTEC: Data Preprocessing

As introduced in Section 5.2, the derivation of DORIS-based altimetry VTEC can be divided into two main components: data preprocessing and interpolation. This section will focus on the comparison of parameters for data preprocessing, while interpolation methods will be addressed in the subsequent section. In addition to the time division and space division methods for data selection, this section will also examine the impact of different elevation masks on the results. Based on a comparative analysis, this section will select an optimal combination of preprocessing parameters for subsequent interpolation, considering the following factors:

- Data Coverage Percentage

Considering the discontinuity in DORIS observations for each revolution of Jason-3 (as shown in Figure 3.2), there are altimetry IPP for which no nearby DORIS VTEC data is available to support ionospheric correction. Specifically, for altimetry IPPs on a given day, only a subset of the points will have DORIS-based altimetry VTEC results. The percentage information derived from this will be used to assess the coverage range of the parameter combination.

- Difference with dual-frequency altimetry VTEC

The altimetry module onboard Jason-3 supports dual-frequency signal transmission, enabling it to provide VTEC information directly at the altimetry IPP location. By using this VTEC information as a reference and comparing it with DORIS-based altimetry VTEC obtained through various preprocessing parameters, the RMS value of the difference between the two can be calculated. This RMS result will serve as an indicator to evaluate the accuracy of each parameter.

Figure 6.5 presents the relationship between the data coverage percentage and RMS difference with results obtained using various parameter combinations at 2023 DOY 221. Specifically, this figure uses space division to obtain RMS-data coverage results under different elevation masks and window sizes.

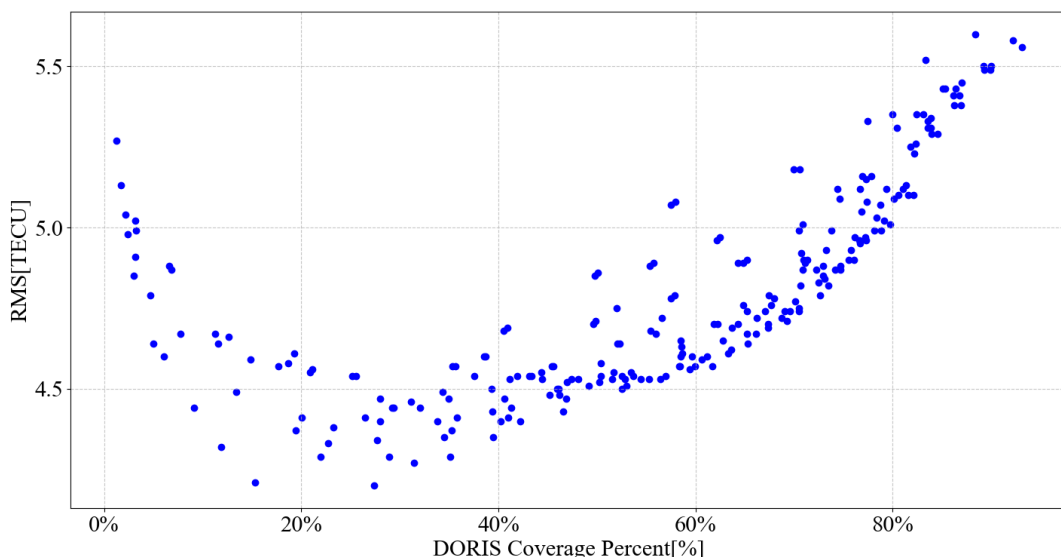


Figure 6.5 Balance in Coverage and Accuracy for Various Elevation Masks and Window Sizes at 2023 DOY 221

As observed, when coverage exceeds 20%, a higher coverage percentage leads to reduced accuracy for DORIS-based altimetry VTEC. This is because achieving higher data coverage requires coarser filtering of DORIS VTEC data, which reduces the quality of DORIS VTEC values available for interpolation. Con-

versely, when coverage falls below 20%, strict filtering of DORIS VTEC data leaves too few interpolation points, similarly diminishing the accuracy of results. Given that very low DORIS data coverage limits the practicality of this correction, this study focuses on the right side of the curve, aiming to find the optimal parameter combinations at a coverage level of 50%. In this section, IDW is employed as the interpolation method.

6.2.1 Data Used for Parameter Evaluation

The results in this section will be derived from data from two groups, each spanning one week. Based on the trends of the F10.7 Index in Figure 2.2, this section will select two time periods representing quiet and active ionospheric conditions for further analysis.

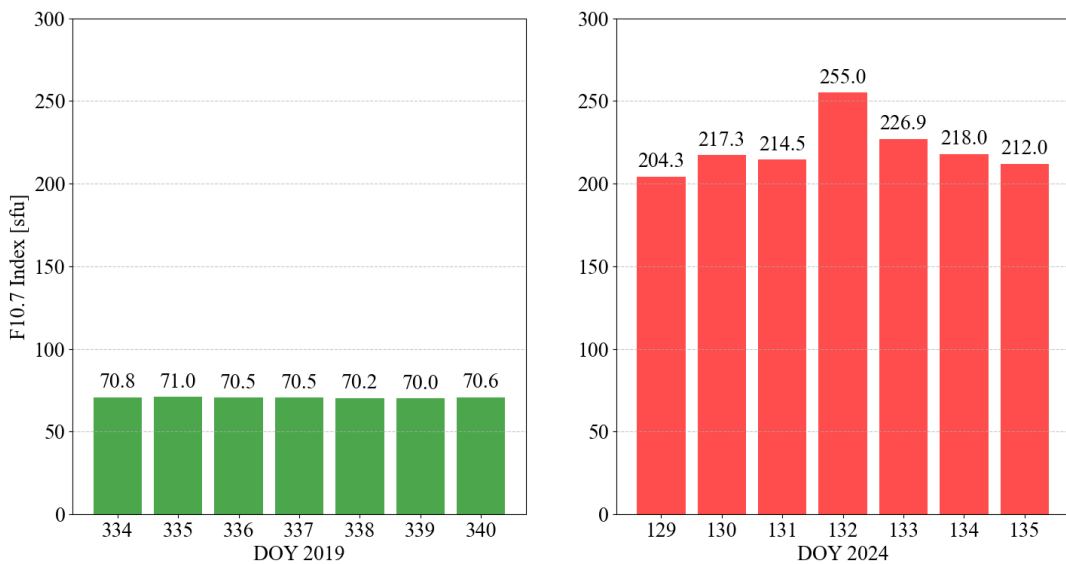


Figure 6.6 F10.7 Index for Quiet and Active Ionospheric Conditions

The subfigure on the left shows the F10.7 index between DOY 334-340 at 17:00 UTC in 2019, while the image on the right depicts the F10.7 index between DOY 129-135 at 18:00 UTC in 2024. It is obvious that the index on the left exhibits very little variation with lower absolute values. In contrast, the index in the right figure has significantly higher absolute values and shows larger fluctuations. During this week, an ionospheric storm event occurred from 16:00 UTC at DOY 131 to the early hours of DOY 132.

Using DORIS observation data from these two different periods, the number of DORIS and altimetry VTEC observations obtained also varies, as shown in Figure 6.7.

The two curves in each sub-figure represent the number of data points for DORIS VTEC and altimetry VTEC for one day, with a total of 54 DORIS stations for both periods. Notably, the DORIS VTEC curve reflects non-interpolated values, corresponding only to the VTEC measurements at DORIS IPP points obtained directly from DORIS observations. It can be observed that, regardless of the ionospheric activity level, the number of Altimetry observations remains stable, at around 55,000 per day. In contrast, the number of DORIS VTEC observations varies significantly during periods of different ionospheric activity, with more data points for the quiet ionospheric period. There are two main reasons for the difference of approximately 13,000 data points. First, during periods of high ionospheric activity, the observation conditions deteriorate, leading to poor temporal continuity in observations and the inability to form complete

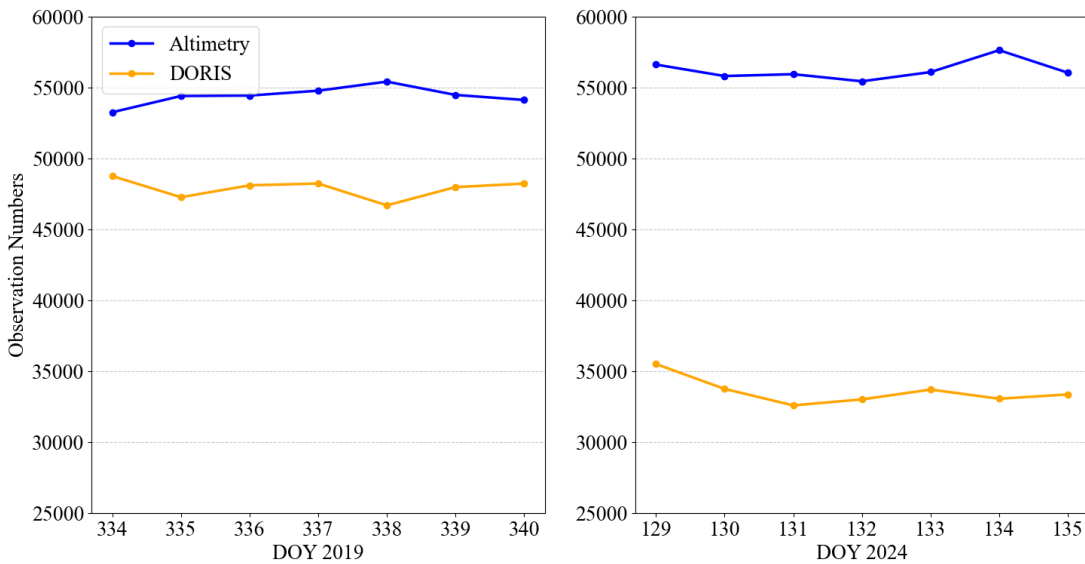


Figure 6.7 DORIS VTEC Observation Numbers for Quiet and Active Ionospheric Conditions

passes (at least 50 consecutive observations are needed to form an individual pass), accounting for about 60% of the missing data. Additionally, the high ionospheric activity causes fluctuations in TEC values, which can be mistakenly identified as cycle slips in the time-difference detection process, leading to around 30% of the data being discarded.

6.2.2 Elevation Mask

The elevation mask is an independent parameter from time division or space division, and its impact on DORIS VTEC data is universal. Therefore, regardless of which division strategy is employed, variations in the elevation mask are expected to have a similar impact on the results. Thus, the discussion on elevation will be addressed first, and five different masks from 0 to 20 degrees will be examined. In the comparison of elevation masks, the other parameters in data selection are kept the same.

- Quiet Condition

Figure 6.8 shows the variation in the RMS values of difference results for different elevation masks under quiet ionospheric conditions. In the figure, the eight lines correspond to the RMS values for 2019 DOY 334-340, and the average value of the week (shown in red). Each line consists of five points representing elevation masks of 0, 5, 10, 15, and 20 degrees, and are located from right to left on the curve respectively. From the trend of each line we can see that with an increased elevation mask or a stricter data filter, a smaller coverage percentage value can be found. It is also evident that during the week of quiet ionospheric conditions, a larger elevation mask allows the DORIS-based altimetry results to have a smaller difference with the dual-frequency altimetry results, leading to a smaller RMS value. This trend is reasonable, as a smaller elevation angle results in a more oblique propagation path, leading to a longer propagation distance. And thus introducing more errors in the traveling path.

For Jason-3 which operates in a near-circular low Earth orbit, the change of geometric relationship with the variation of the elevation angle is illustrated in Figure 6.9. Considering that Jason-3 orbits

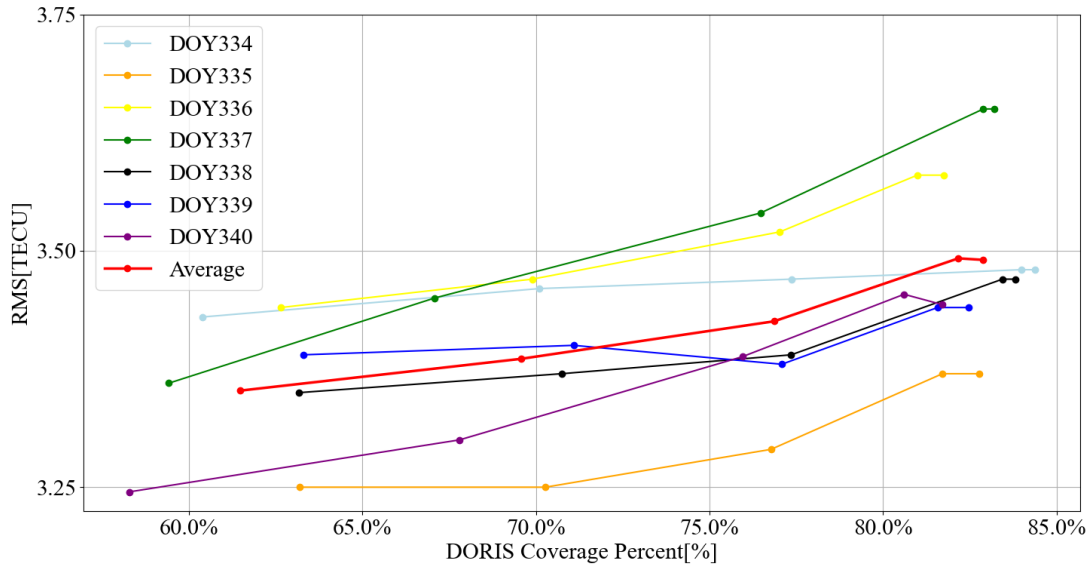


Figure 6.8 DORIS VTEC RMS values for Different Elevation Masks in Quiet Condition

at an altitude of $h_{\text{sate}} = 1350$ km, the maximum length of the path where the elevation angle is 0 degrees can exceed 4300 km, which is three times the length for a 90-degree elevation angle.

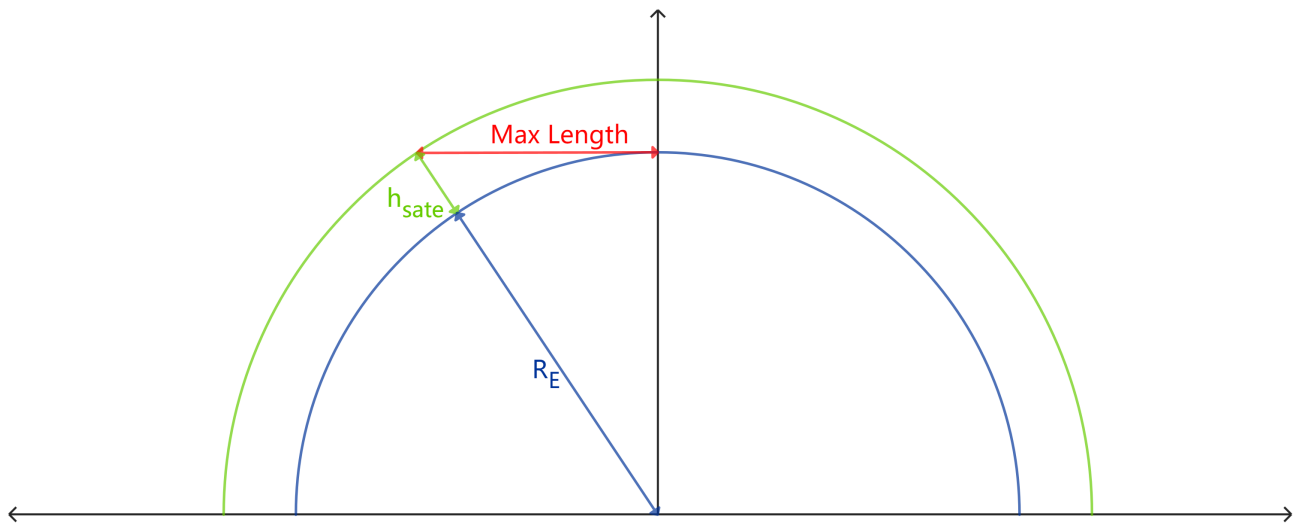


Figure 6.9 Illustration of Elevation-dependent Geometry

- Active Condition

Figure 6.10 illustrates the impact of the elevation mask on both data coverage and RMS values during the active ionospheric period of 2024 DOY 129-135. The larger fluctuations in the ionosphere diminish the clarity of the influence that the elevation mask has on the RMS trend. This is most apparent at DOY 131. Due to the occurrence of the ionospheric storm, the blue curve for DOY 131 exhibits the highest RMS value over the seven-day period, and the relationship between its accuracy and the elevation mask is also the least evident. However, the red curve still indicates that, on a larger timescale average, a higher elevation mask corresponds to improved observation quality. Additionally, from the perspective of data coverage, the percentage of DORIS correction

during the active ionospheric period is overall lower compared to the percentage data in Figure 6.8, which represents quiet conditions. The percentage difference is about 20% for each elevation mask. The difference in data coverage is also due to the reduced number of DORIS passes under active ionospheric conditions, as illustrated in Figure 6.7.

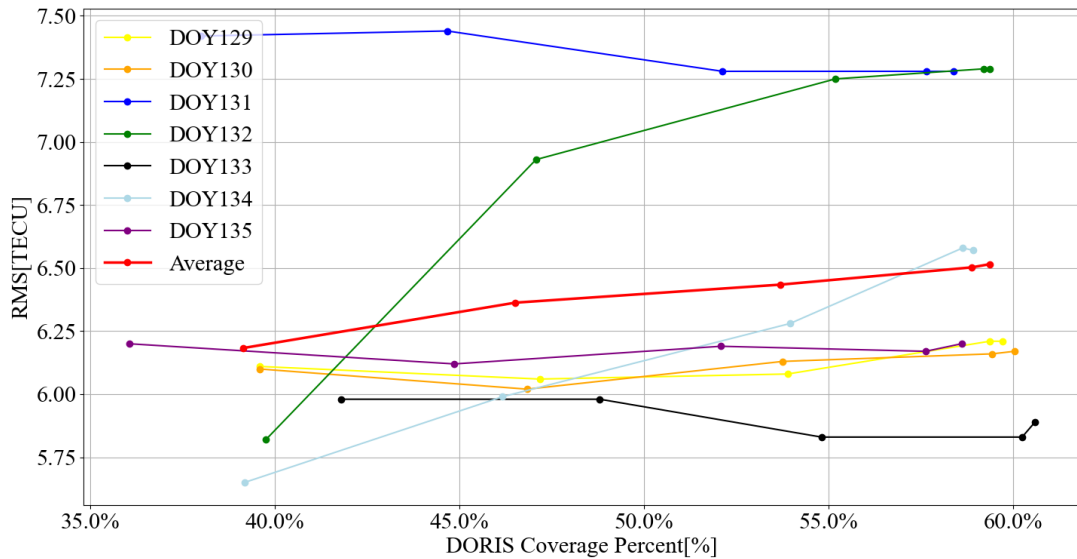


Figure 6.10 DORIS VTEC RMS for Different Elevation Masks in Active Condition

From the point distribution of both Figure 6.8 and 6.10, it can be observed that using elevation masks of 0° and 5° (the two points at the right end of the curve) results in only a minor difference in data coverage. This is partly due to the challenging observation conditions at very low elevation angles, leading to data termination, and partly because atmospheric refraction may cause the propagated signal to bend toward the ground, preventing it from being received by satellite for the near-zero elevation satellite-ground station link.

Overall, from the average curve, it can be observed that larger elevation masks lead to improved DORIS data quality and more accurate RMS results but are accompanied by a lower data coverage percentage. In the following analysis of the division strategy, a 10° elevation mask — similar to that commonly used in GNSS — will be adopted as the basis for comparison.

6.2.3 Parameters in Space Division

The following two subsections will discuss the data coverage and RMS for the two division strategies described in Subsection 5.2.1. Through comparison, the optimal parameter combination will be finally identified. This subsection will first introduce the parameter combinations for the space division approach.

When using space division to select DORIS observations near the altimetry IPP, we need to define a neighborhood, essentially a window centered on the altimetry IPP, within which we also aim to include a sufficient number of DORIS observations for subsequent interpolation. Consequently, this process involves two types of parameters: the window size and the observation quantity threshold within the window.

For the selection of the window size, this thesis will use a rectangular grid where the latitude span is half that of the longitude, e.g. 1° (latitude) \times 2° (longitude). The reason for this can be divided into the following points. From a data processing perspective, this simplified shape significantly reduces the number of

window types and sizes we need to compare, making it easier to select an accurate option from among various window sizes. In terms of ionospheric variation, as shown in Figure 2.5, the VTEC values exhibit more significant changes in the latitudinal direction than in the longitudinal direction, and it is reasonable to use a smaller latitudinal range to define the neighborhood around the altimetry IPP. Additionally, the GIM product from GNSS also uses a similar grid, with the size of each unit being 2.5° (latitude) $\times 5^\circ$ (longitude) to cover the global range. In this study, seven region sizes ranging from $1^\circ \times 2^\circ$ to $7^\circ \times 14^\circ$, will be compared.

Moreover, the threshold for the number of DORIS observations within the window should also be a variable parameter that adjusts with window size. For a larger window, a higher threshold can be set to ensure better data coverage and a more evenly distributed DORIS IPP across the window region. Conversely, a smaller window inherently contains fewer DORIS observations, so a lower count threshold is necessary to maintain comparable data coverage. The following part will analyze the accuracy and data coverage of these two key parameters under both quiet and active ionospheric conditions.

- Quiet Condition

The relationship between the minimum observation numbers and data coverage in quiet ionospheric conditions can be found in Figure 6.11.

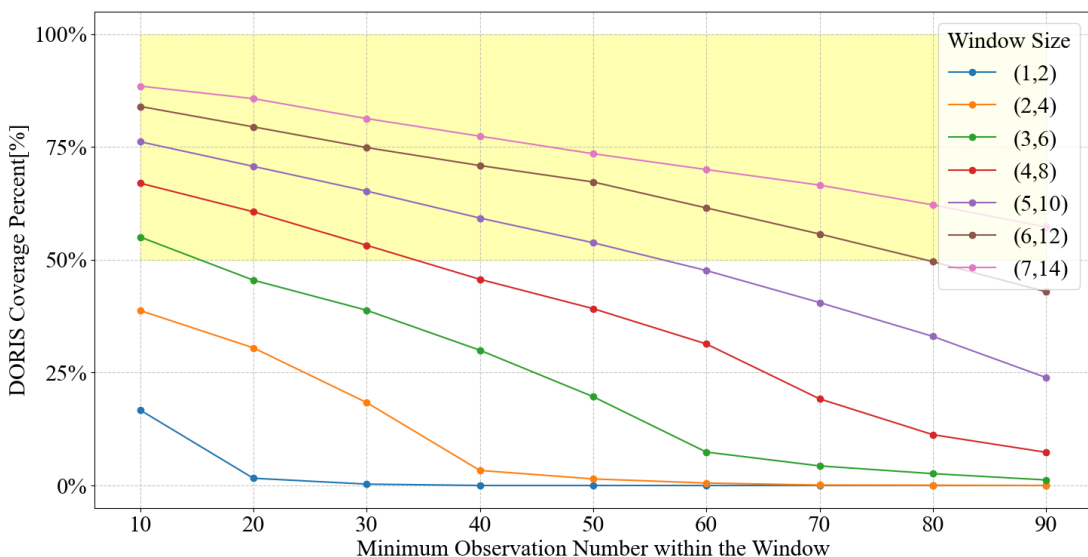


Figure 6.11 Relation between Threshold of Obs Number and VTEC RMS in Quiet Condition at DOY 334

The figure contains seven curves, representing the results for seven window sizes. The x-axis shows the minimum observation numbers required within the window, varying from 10 points to 90 points, and the y-axis is the data coverage percentage. From the overall trend of the curve in the figure, it can be observed that a bigger window size indicates a better data coverage percentage, as the higher the curve, the larger the window size it represents. Besides, an increase in minimum observation numbers means a decrease in data coverage percentage. This relationship aligns with the discussion above. As mentioned in the introduction part of this section, the analysis of data accuracy in this thesis will be based on 50% coverage of DORIS-based altimetry VTEC, which corresponds to the yellow region in the figure.

Given that a small window size cannot achieve a high level of data coverage (e.g., for a window size of (2, 4), the maximum coverage does not exceed 40%), this section will compare five parameter combinations as shown in Table 6.2 that achieve a weekly averaged data coverage of 50%.

Table 6.2 Parameters and Averaged Coverage for Quiet Condition

| Window Size [°] | (3,6) | (4,8) | (5,10) | (6,12) | (7,14) |
|-----------------|-------|-------|--------|--------|--------|
| Min Obs Num | 10 | 30 | 50 | 70 | 90 |
| Coverage [%] | 55.0 | 53.2 | 53.8 | 55.7 | 57.3 |

For all the five parameter combinations in Table 6.2, the data coverage is around the same 50%. Using this similar percentage as a baseline, the accuracy of the DORIS-based altimetry VTEC for these parameter combinations is shown in Figure 6.12.

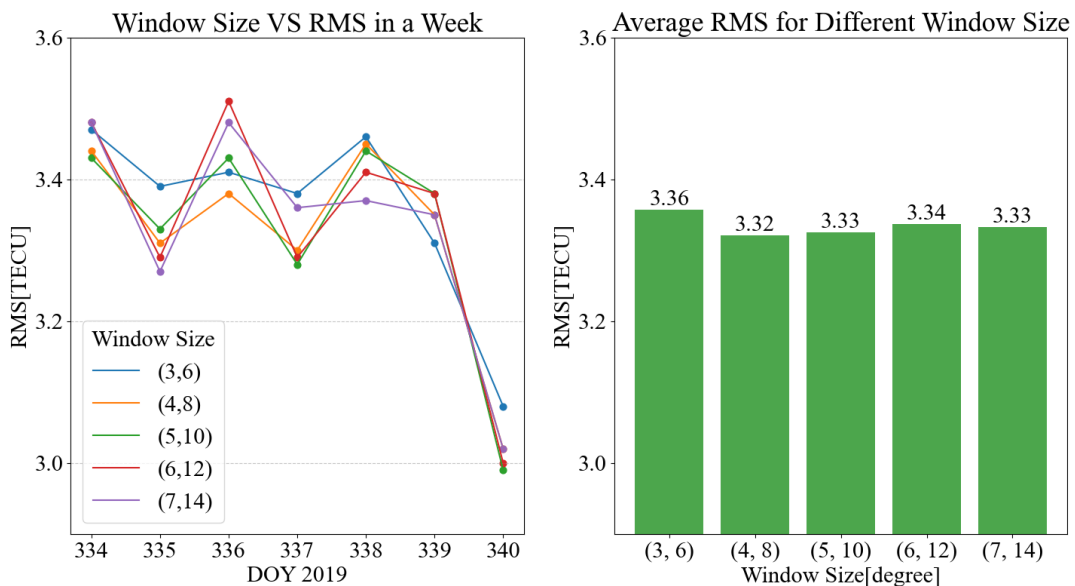


Figure 6.12 RMS Variation for Different Window Size in Quiet Ionospheric Condition

The figure on the left illustrates the variation of RMS over one week for the five different parameter combinations. The figure on the right reflects the average RMS over the same week for these combinations. Comparing DORIS-based altimetry VTEC with altimetry VTEC, the RMS variation is small during periods of low ionospheric activity, around 3 to 3.5 TECU. Similarly, on the right, the average RMS among the different parameter combinations shows only minor differences throughout the week, with the minimum appearing in the window size of (4,8). This indicates that during quiet periods, the influence of window size in the window on the result accuracy is small with a similar data coverage of around 55%.

In fact, under quiet ionospheric conditions, using different data coverage standards or adjusting the minimum observation threshold within the window also does not significantly impact the accuracy of the results. Table 6.3 presents the variation in mean RMS with data coverage at 2019 DOY 334. The window size remains fixed at (7, 14), while the minimum number of observations within the window changes from 10 to 90, thereby altering the coverage percentage and accuracy. However, the small variation of RMS indicates that the differences in the parameter have a small impact on accuracy for quiet ionospheric condition.

Table 6.3 Relation of Coverage and RMS in Quiet Condition with (7,14) Window at 2019 DOY 334

| Min Obs Num | 10 | 20 | 30 | 40 | 50 | 60 | 70 | 80 | 90 |
|--------------|------|------|------|------|------|------|------|------|------|
| Coverage [%] | 88.5 | 85.7 | 81.3 | 77.4 | 73.5 | 70.0 | 66.6 | 62.4 | 57.3 |
| RMS [TECU] | 3.47 | 3.47 | 3.47 | 3.47 | 3.47 | 3.46 | 3.46 | 3.48 | 3.48 |

- Active Condition

As illustrated in Figure 6.7, the data coverage percentage during active periods show an overall decrease compared to quiet periods, and under these conditions, only the last four window sizes meet the 50% data coverage requirement, as shown in Figure 6.13.

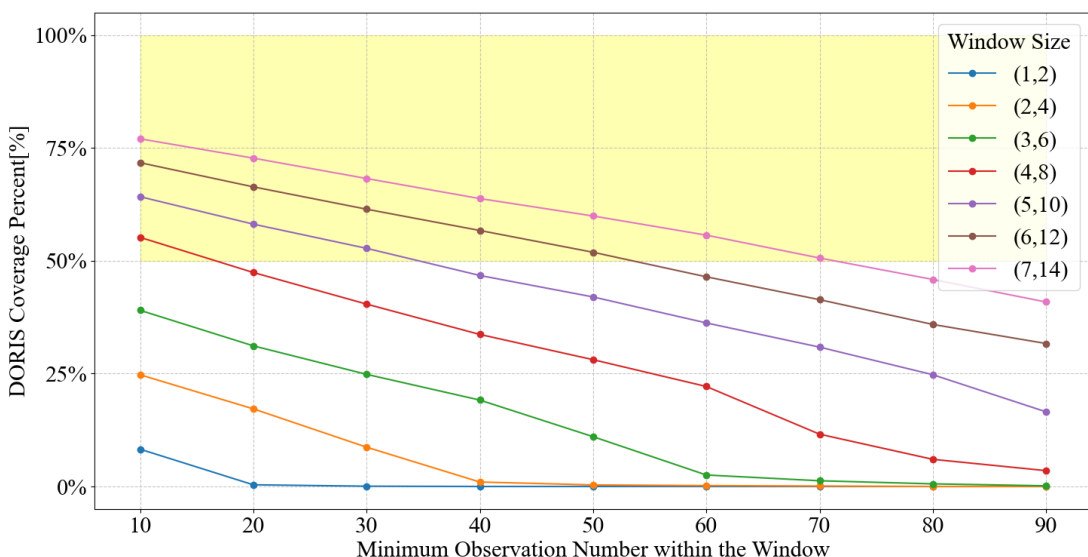


Figure 6.13 Relation between Threshold of Obs Number and VTEC RMS in Active Condition at DOY 334

The specific parameter combinations, with the averaged coverage percentage over the week, are shown in Table 6.4.

Table 6.4 Parameters and Averaged Coverage for Active Condition

| Window Size[°] | (4,8) | (5,10) | (6,12) | (7,14) |
|----------------|-------|--------|--------|--------|
| Min Obs Num | 10 | 30 | 50 | 70 |
| Coverage [%] | 54.6 | 52.6 | 52.0 | 51.2 |

Figure 6.14 shows the RMS results for the four different window sizes. From the left figure, it can be seen that during the active week, the RMS results fluctuate more significantly between different days, and the accuracy also varies across different window sizes. The peak RMS value appears at DOY 131, during which period the ionospheric storm happens. The right figure shows the weekly average, and the difference between different window sizes is more pronounced, with (5,10) being the most accurate size overall. Also, we can see that using a larger window results in an accuracy decline of more than 0.1 TECU. This trend, which contrasts sharply with the quiet conditions, indicates that during periods of high ionospheric activity, the fluctuating ionospheric conditions within a larger window cannot accurately reflect the VTEC values at the altimetry IPP location.

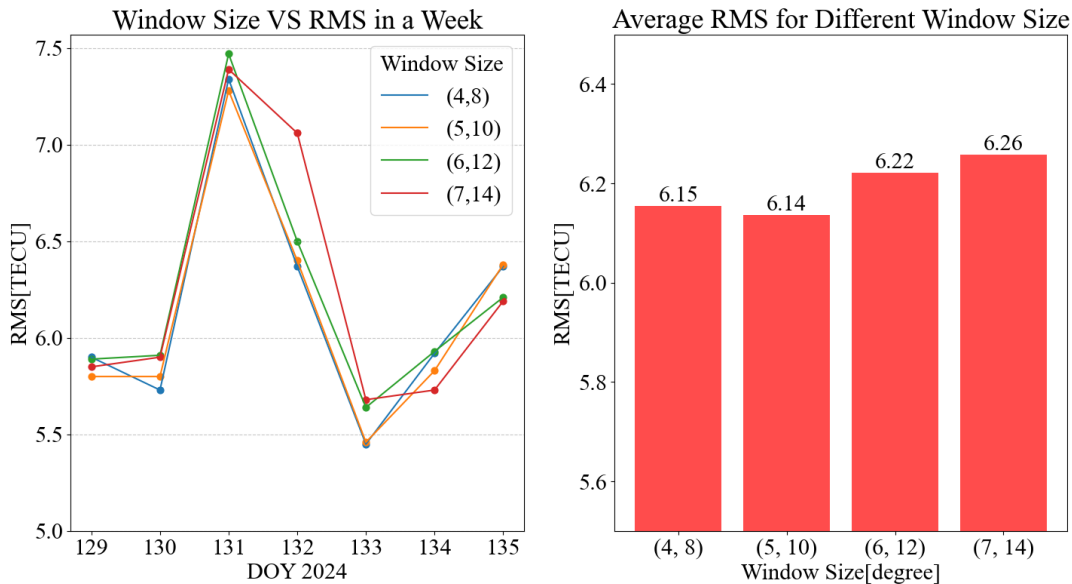


Figure 6.14 RMS Variation for Different Window Size in Active Condition

In this subsection, we compared the DORIS-based altimetry VTEC with dual-frequency altimetry VTEC across different levels of ionospheric activity and parameter combinations. The results show that during periods of low ionospheric activity, different parameter combinations did not result in significant changes in accuracy. However, during periods of high ionospheric activity, a smaller window size combined with a lower minimum observation number in the window yielded smaller RMS values.

Following the optimal results given in Figure 6.12 and Figure 6.14, the parameter combinations in the data preprocessing part will be :

Table 6.5 Parameter Combination for Two Conditions in Space Division

| | Quiet Condition | Active Condition |
|------------------------|------------------------|-------------------------|
| Elevation [°] | 10 | 10 |
| Window Size [°] | (4,8) | (5,10) |
| Min Obs Num | 30 | 30 |

6.2.4 Parameters in Time Division

When selecting DORIS VTEC near the altimetry IPP with time division, it is necessary to choose a time interval centered around the altimetry IPP and use the DORIS observations within this interval, as well as to determine the minimum DORIS observation numbers within this interval.

In this thesis, five different time intervals — 1, 2, 3, 4, and 5 minutes — will be used for comparison. Jason-3, operating at a near-circular orbit with a radial velocity of approximately 7185 m/s, will cover about 19 degrees of latitude or longitude (at the equator) within 5 minutes. This value slightly exceeds the distance traversed by the satellite in the (7, 14) window. In one minute, it covers approximately 4 degrees in latitude, roughly corresponding to the distance the satellite travels within the (2, 4) window. This correspondence serves as the foundation for comparing the accuracy of time and space division strategies.

- Quiet Condition

Similar to space division, the relationship between the minimum observation number and data coverage percentage for time division is shown in Figure 6.15, with different curves having different time interval settings.

Overall, it exhibits a trend similar to what is illustrated in Figure 6.11, where larger data coverage is achieved with a smaller observation number threshold. However, as seen from the x-axis of Figure 6.15, time division allows significantly more DORIS observation points than space division. The reason why fewer observation numbers are allowed for space division is that the spatial relation between a fixed-size, fixed-direction space window, and the satellite's ground track varies in each revolution, and the numbers of DORIS observations in the window also change depending on the satellite's position. In contrast, time division consistently selects DORIS VTEC observations within a specific time interval, making the number of observations much more stable. Consequently, the average observation number over one day will be higher for time division, even if both time and space division cover a similar proportion of the satellite orbit.

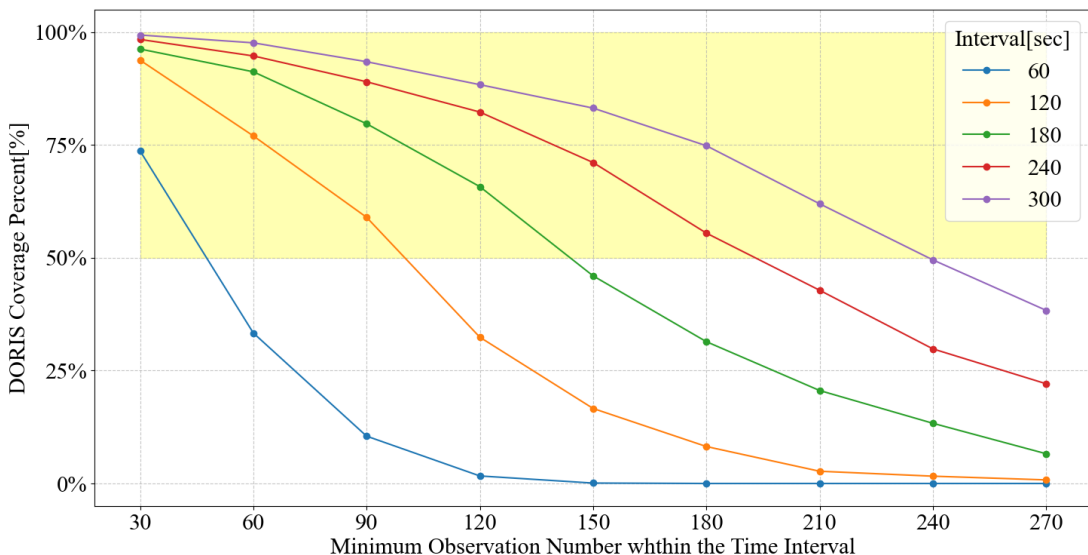


Figure 6.15 Relation between Threshold of Obs Number and VTEC RMS in Quiet Condition at DOY 334

Using 50% data coverage as the base, we select the following parameter combinations, as shown in Table 6.6, and the corresponding accuracy comparison is presented in Figure 6.16.

Table 6.6 Parameter combinations and data coverage percentages for Quiet Condition

| Time Interval [sec] | 60 | 120 | 180 | 240 | 300 |
|---------------------|------|------|------|------|------|
| Min Obs Num | 50 | 100 | 140 | 180 | 225 |
| Coverage [%] | 58.2 | 53.7 | 53.1 | 55.5 | 55.7 |

Similar to space division, during the week of low ionospheric activity, using different parameter combinations does not significantly impact the RMS results. The only notable accuracy deviation of 0.05 TECU occurs with the largest interval of 300 seconds for the right figure.

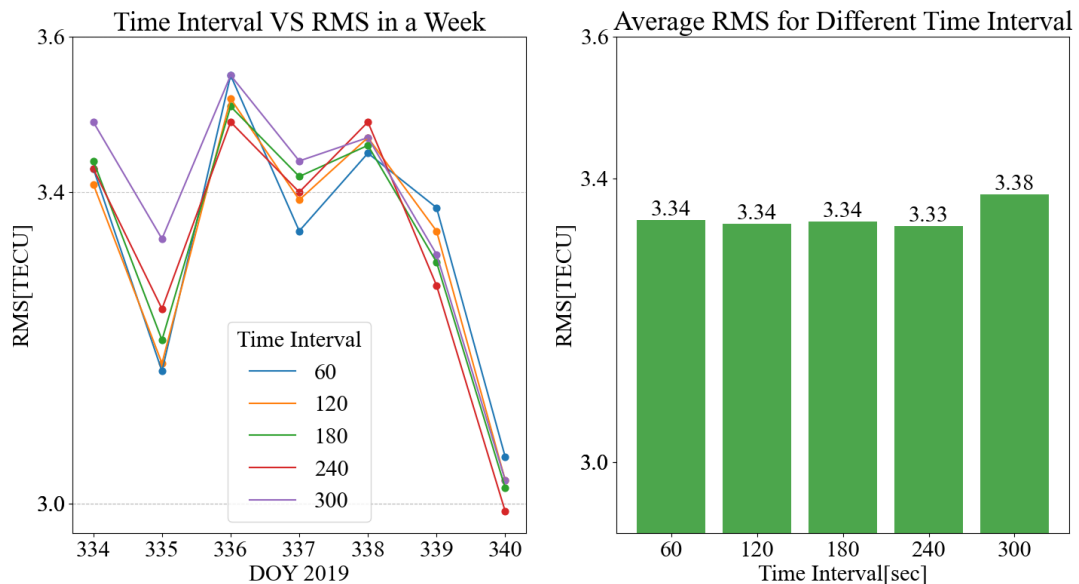


Figure 6.16 RMS Variation for Different Time Intervals in Quiet Condition

- Active Condition

The time division parameter combinations that achieve 50% data coverage in active ionosphere conditions are shown in Figure 6.17 and Table 6.7.

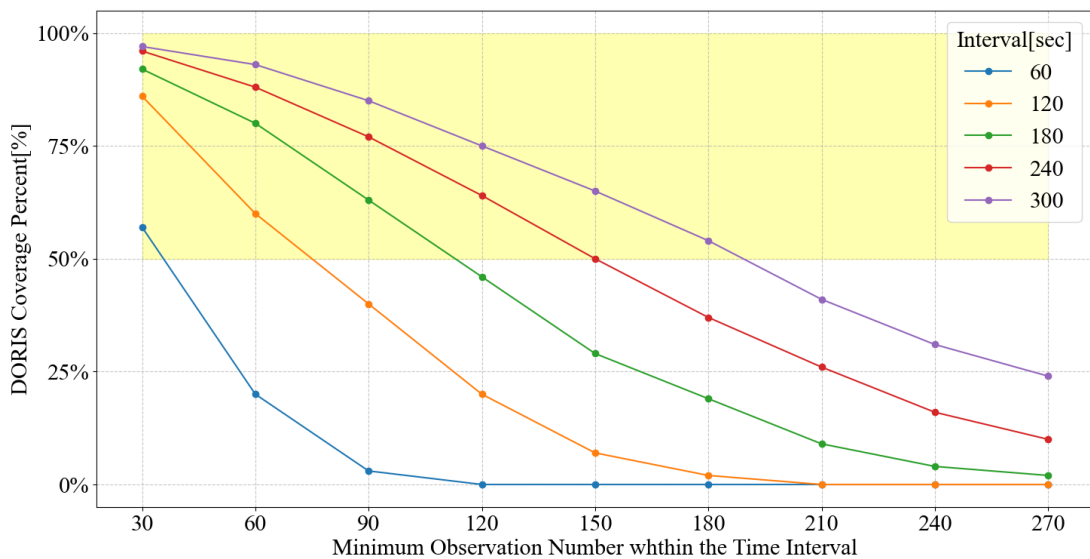


Figure 6.17 RMS Variation for Different Time Intervals in Active Condition

Table 6.7 Parameter combinations and data coverage percentages for Active Condition

| Time Interval [sec] | 60 | 120 | 180 | 240 | 300 |
|---------------------|------|------|------|------|------|
| Min Obs Num | 35 | 75 | 110 | 150 | 180 |
| Coverage [%] | 52.3 | 50.3 | 52.0 | 50.2 | 54.0 |

Figure 6.18 illustrates the variation in RMS results for the corresponding parameter combinations over a week, as well as a weekly average comparison across different combinations. From the left figure, it can be seen that the accuracy curve varies by more than 1 TECU over time. The largest deviation from dual-frequency altimetry VTEC occurs during the two days of DOY 131 and 132, which also coincides with the ionospheric storm.

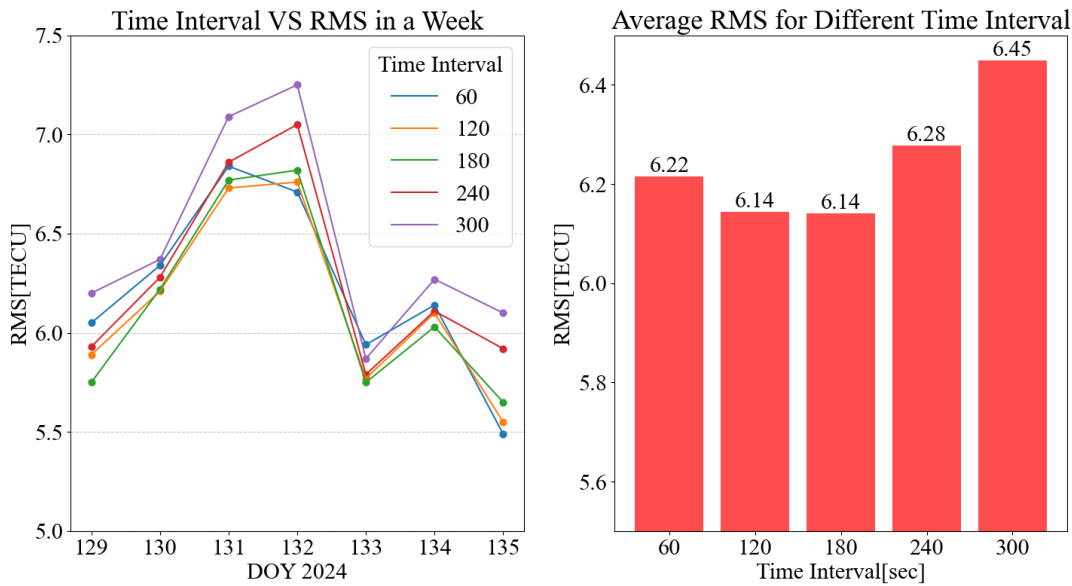


Figure 6.18 RMS Variation for Different Time Intervals in Active Condition

In terms of differences between parameter combinations, the purple line (300-second interval) shows notably lower accuracy compared to the other curves. This is more evident in the right figure, where the weekly average indicates that the RMS mean for the 300-second interval is the highest and significantly larger than other parameter combinations. Additionally, the right figure also reveals that under active ionospheric conditions, after exceeding a certain interval, the accuracy decline correlates with the increasing length of the interval.

Generally speaking, using time division allows for a higher number of observations compared to space division when achieving similar data coverage. Combining the results from quiet and active conditions as shown in Figure 6.16 and Figure 6.18, it is evident that the 300-second interval experiences a significant accuracy decline compared to other parameter combinations in time division. This suggests that the additional DORIS VTEC observations obtained with a larger interval are no longer representative of the ionospheric region near the altimetry IPP. During periods of active ionospheric activity, the appropriate interval size is smaller than during quiet periods, with accuracy decline already appearing at the 240-second interval.

Based on the optimal RMS results from both figures, the optimal parameter combinations for the two different ionospheric conditions can be determined, as shown in Table 6.8.

6.2.5 Comparison of Two Division Strategies

The previous two subsections presented the accuracies of two different parameter selection strategies. Using the best-performing parameter combinations from each strategy in Table 6.5 and 6.8, the accuracy of the DORIS-based altimetry VTEC is shown in Table 6.9. It is worth noting that time and space divisions

Table 6.8 Parameter Combination for Two Conditions in Time Division

| | Quiet Condition | Active Condition |
|----------------------------|------------------------|-------------------------|
| Elevation [°] | 10 | 10 |
| Time Interval [sec] | 240 | 120 |
| Min Obs Num | 180 | 75 |

have a roughly similar processing load for optimal parameter settings, and the computation of DORIS-based altimetry VTEC for a day takes approximately 30 seconds.

Table 6.9 Accuracy of VTEC for Two Division Strategies

| | Quiet Condition | Active Condition |
|------------------------------|------------------------|-------------------------|
| Space Division [TECU] | 3.32 | 6.06 |
| Time Division [TECU] | 3.33 | 6.14 |

From the comparison, it is evident that during periods of high ionospheric activity, the space division method yields better estimation results, while both methods perform similarly during quiet periods. The less ideal performance of time division during active periods may be related to its data selection approach. As shown in Figure 4.2, the trajectory of Jason-3 with a non-zero orbital inclination, constantly changes its direction through the ionosphere within one cycle. In high-latitude regions where ionospheric variation is slower, the trajectory primarily follows the meridional direction, while in low-latitude regions with faster ionospheric changes, it moves predominantly along the latitudinal direction. Considering the larger variability in the ionosphere along latitude, the DORIS VTEC selected by time division in low-latitude areas may span different ionospheric activity regions, potentially impacting the accuracy of DORIS-based altimetry VTEC.

In summary, time division allows for the acquisition of more DORIS VTEC observations within a similar range; however, space division achieves better accuracy of elevation and division strategy. The parameter combination selected for data preprocessing will be as follows: an elevation angle of 10 degrees, a window size of (4,8) for quiet condition and (5,10) for active condition, and a minimum observation number of 30 for both.

6.3 DORIS-based Altimetry VTEC: Interpolation

Section 5.2.2 introduced two interpolation methods: IDW and Kriging. Using the DORIS VTEC values selected with the parameters from the last section, this section will compare the accuracy of the two interpolation methods over the same two quiet and active periods.

Figure 6.19 shows the accuracy results for the IDW (blue) and Kriging (orange) interpolation methods under quiet (top) and active (bottom) ionospheric conditions.

The weekly average RMS data obtained from the figure is shown in Table 5.9. It indicates that the accuracy difference between IDW and Kriging interpolation is insignificant, not exceeding 0.1 TECU for the same data set even under active ionospheric conditions.

Overall, compared to different parameter choices in preprocessing, the interpolation method has an insignificant impact on the final DORIS-based altimetry VTEC results. However, IDW is a simpler interpolation algorithm compared to Kriging, which is also reflected in their processing times. IDW takes approximately 30 seconds to process one day's data using the same parameter combinations, whereas Kriging

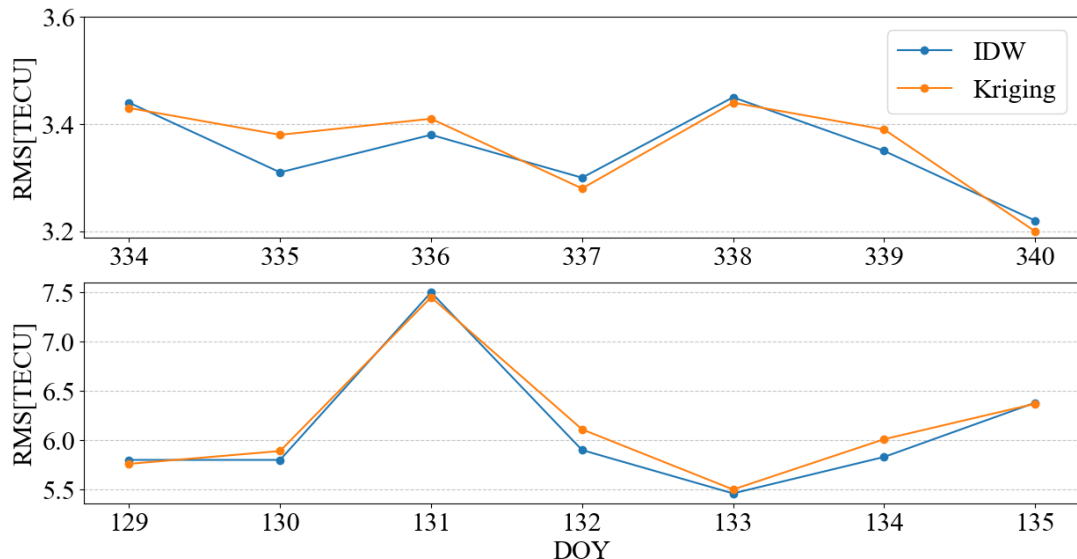


Figure 6.19 VTEC RMS for Two Interpolation Methods

Table 6.10 Average VTEC RMS for Two Interpolation Methods

| | Quiet Condition | Active Condition |
|----------------|-----------------|------------------|
| IDW [TECU] | 3.35 | 6.10 |
| KRIGING [TECU] | 3.36 | 6.16 |

with a linear fitting function requires about 180 seconds. Therefore, IDW will be used as the interpolation method for comparison with GIM in the subsequent validation analysis.

6.4 DORIS-based altimetry VTEC: Comparison with GIM

In this section, using the optimal parameter combination and interpolation method identified previously, we will evaluate the accuracy of the DORIS-based altimetry VTEC. Here, we will similarly use the RMS of the difference between it and the dual-frequency altimetry VTEC as the accuracy metric. Additionally, two GIM-referenced VTEC will be included for comparison. The GIM model used here is provided by IGS.

- GIM-based Altimetry VTEC

Using the IGS GIM product to acquire the VTEC values located at the altimetry IPP, we get GIM-based altimetry VTEC. For altimetry, IPP coordinates that are not located on the GIM grid points, temporal and spatial interpolation will be applied as outlined in Equation (5.1). The final results will also be adjusted according to Jason-3 scale factors specified in Table 5.1.

- GIM-interpolated Altimetry VTEC

The process to obtain GIM-interpolated altimetry VTEC involves three steps: first, we need to obtain the DORIS IPP location information for those preprocessed DORIS observations on which elevation mask and space division are applied; second, using the IGS GIM product, and based on the DORIS IPP information from the previous step, we obtain the GIM VTEC values at DORIS IPP locations through interpolation and scaling factor adjustment introduced in Section 5.1; finally, we can get the

GIM-interpolated VTEC result by applying the same preprocessing and interpolation approaches introduced in the last four Sections.

Using GIM-based altimetry VTEC to correct ionospheric delay is currently a common correction approach for single-frequency altimetry satellites. By comparing DORIS-based altimetry VTEC with it, we can analyze the feasibility of using DORIS for VTEC correction from an accuracy perspective. Additionally, comparing DORIS-based altimetry VTEC with the similarly derived GIM-interpolated altimetry VTEC allows us to eliminate accuracy differences arising from the unique characteristics of the DORIS-based altimetry VTEC retrieval method, and further we can evaluate the accuracy between DORIS observations and the IGS GIM product at DORIS IPP locations .

As in previous sections, the comparison will also be conducted based on both quiet and active ionospheric periods. The comparison period spans 30 days, ranging from DOY 334 to DOY 353 in 2019 for quiet conditions and from DOY 129 to DOY 158 in 2024 for active conditions. This longer period provides a more stable assessment of the accuracy of different VTEC products and their correlation with each other.

The F10.7 index of the two periods is shown in Figure 6.20. In the active condition, the index shows fluctuations exceeding 100 TECU, while in the quiet condition, it remains highly stable with overall fluctuations not exceeding 5 TECU.

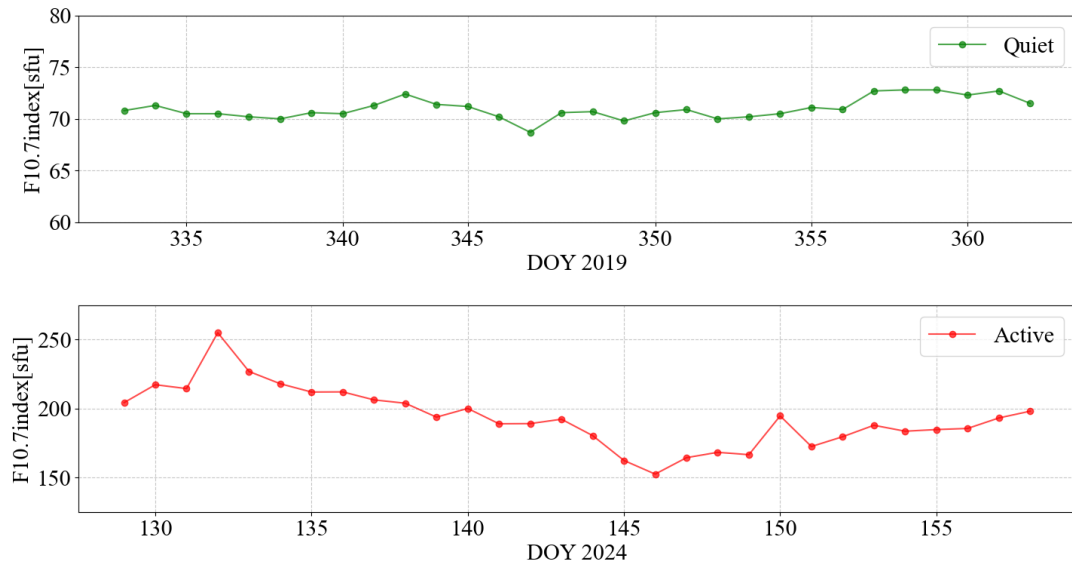


Figure 6.20 Variation of F10.7 Index in Quiet and Active Conditions

- Quiet Condition

Figure 6.21 shows the variation in RMS differences between the three correction methods and dual-frequency altimetry VTEC over a month under ionospheric quiet conditions.

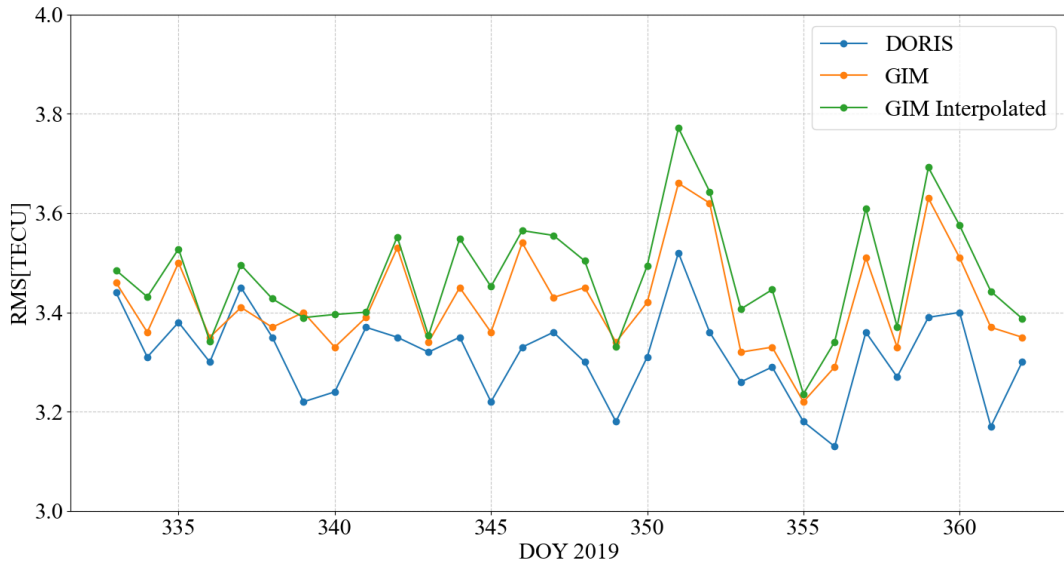


Figure 6.21 Comparison of RMS values for DORIS and GIM in Quiet Ionospheric Condition

As shown in the figure, the DORIS curve (blue) maintains the highest accuracy over the 30-day period, while the GIM curve (orange) has slightly lower accuracy compared to DORIS, and the GIM interpolated curve (green) performs least ideal over the month. The average RMS values in the thirty days for these three approaches are listed in Table 6.11.

Table 6.11 Average RMS values for DORIS and GIM VTEC Corrections in Quiet Condition

| | DORIS-based VTEC | GIM-based VTEC | GIM-interpolated VTEC |
|------------|------------------|----------------|-----------------------|
| RMS [TECU] | 3.31 | 3.42 | 3.45 |

As observed from Figure 6.21 and Table 6.11, over this 30-day period, the DORIS-based altimetry VTEC consistently demonstrates a stable RMS advantage over the GIM results, with a 0.11 TECU advantage in the average result. This indicates that, under quiet ionospheric conditions, DORIS-based altimetry VTEC provides the most accurate estimate of altimetry VTEC of the three. The results of GIM-interpolated are slightly larger than those of GIM-based, indicating that multiple interpolations lead to a certain loss of accuracy. Additionally, the 0.14TECU difference between GIM-interpolated and DORIS results highlights that, at DORIS IPPs, DORIS observations provide more accurate VTEC values compared to GIM.

However, it is worth noting that GIM provides global VTEC coverage, enabling it to offer GIM-based altimetry VTEC at 100% of the altimetry IPP locations. In contrast, the results obtained using DORIS interpolation cover 50% of the altimetry IPP locations.

Table 6.12 Correlation of GIM and DORIS Curves in Quiet Condition

| | GIM-GIM interpolated | DORIS-GIM interpolated | DORIS-GIM |
|-------------|----------------------|------------------------|-----------|
| Correlation | 0.946 | 0.730 | 0.721 |

The correlation between the three curves is illustrated in Table 6.12. From the trend of the three curves, it can be observed that the GIM and GIM interpolated curves are highly correlated with a

correlation of more than 0.9. This is reasonable, considering that they are produced by the same IGS GIM data set, and that little VTEC fluctuation is presented on quiet ionospheric conditions. Besides, due to the similarity in calculation methods, the DORIS curve also exhibits a higher correlation with the GIM interpolated curve than with the GIM curve, which is particularly evident in the period between DOY 344 and DOY 352.

- Active Condition

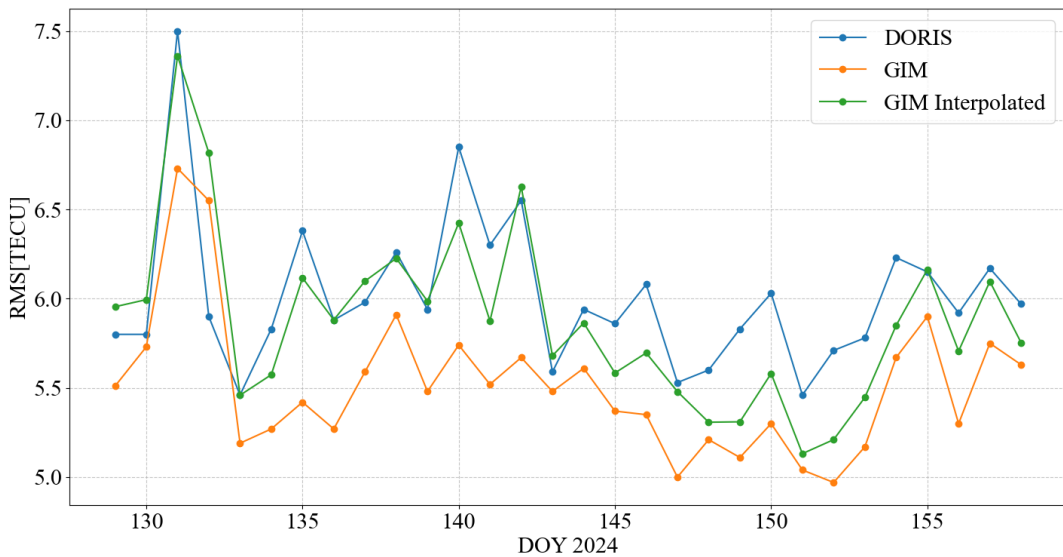


Figure 6.22 Comparison of RMS values for DORIS and GIM in Active Ionospheric Condition

Figure 6.22 shows a comparison of the three results under active ionospheric conditions over the corresponding 30 days. In the figure, the peak RMS values for all three curves appear at DOY 131 and DOY 132, aligning with the ionospheric storm event. In terms of the magnitude of RMS values, the GIM curve in orange achieves higher accuracy compared to the DORIS-based VTEC results (blue) during active ionospheric periods. Both the accuracy and trend of the GIM-interpolated curve (green) are more similar to that of DORIS, as can be seen from the average accuracy Table 6.13.

Table 6.13 Average RMS values for DORIS and GIM VTEC Corrections in Active Condition

| | DORIS-based VTEC | GIM-based VTEC | GIM-interpolated VTEC |
|------------|------------------|----------------|-----------------------|
| RMS [TECU] | 6.01 | 5.52 | 5.88 |

Table 6.14 shows the correlation coefficients among the three curves under the active condition.

Table 6.14 Correlation of GIM and DORIS Curves in Active Condition

| | GIM-GIM interpolated | DORIS-GIM interpolated | DORIS-GIM |
|-------------|----------------------|------------------------|-----------|
| Correlation | 0.917 | 0.808 | 0.687 |

It can be seen that, compared to the quiet condition, the correlation coefficient between the GIM and GIM interpolated curves decreases by a small value of 0.003. Additionally, the RMS difference between the two is larger than in the quiet condition. This indicates that intense ionospheric fluctu-

ations lead to a larger discrepancy between the GIM-interpolated VTEC at the DORIS IPP and the GIM-based VTEC at the altimetry IPP.

However, the correlation coefficient between the DORIS and GIM interpolated curves is higher than in the quiet condition. This indicates a relatively larger similarity between the GIM VTEC and DORIS VTEC at the DORIS IPP. However, as shown by the bar lengths in Figures 6.1 and 6.2 (STEC leveling results), the DORIS VTEC exhibits a larger discrepancy with the corresponding GIM VTEC under the active condition than the quiet condition, reflecting different variation trends in these two data sets. This thesis suggests that the increase in correlation may be due to the rise in the absolute values for these curves. Regarding the absolute difference between the DORIS and GIM interpolated curves, the discrepancy is larger under the active condition. However, the increase in their absolute values could be overshadowing this trend.

Comparing the RMS results under quiet and active ionospheric conditions reveals that DORIS-based altimetry VTEC achieves smaller RMS values than GIM in quiet conditions. In contrast, the opposite is true under active conditions. This phenomenon could be attributed to several factors as listed below.

- Fewer DORIS VTEC Observations

As discussed in Section 5.2.2, under active conditions, the lack of dual-frequency signals and the impact of cycle slip false filtering reduces the number of observations available for the calculation of DORIS VTEC. Consequently, achieving similar data coverage in active conditions requires using less optimal data, reflected in the parameter combination with a larger window size [(5,10) instead of (4,8)].

- Larger Discrepancy between DORIS and Altimetry VTEC

During periods of the active ionosphere, even when using the same window size as in quiet periods to obtain a similar geometric distribution of DORIS IPP locations, it is impossible to achieve accuracy comparable to that in quiet conditions. Table 6.15 lists the average standard deviation of the interpolation points over 30 days for different window sizes under both ionospheric activity levels.

Table 6.15 VTEC STD Values under Quiet and Active Conditions for Different Window Sizes

| Window Size [°] | Condition | |
|-----------------|--------------|---------------|
| | Quiet [TECU] | Active [TECU] |
| (3,6) | 0.56 | 1.46 |
| (4,8) | 0.74 | 1.80 |
| (5,10) | 0.84 | 2.09 |

From the table, we can spot that for the same window size, the interpolation points under active conditions exhibit a significantly larger standard deviation, indicating a larger data discrepancy between DORIS and altimetry VTEC.

In summary, the comparison with GIM VTEC in this section shows that it is feasible to obtain DORIS-based altimetry VTEC using DORIS VTEC during quiet ionospheric conditions. In this scenario, the DORIS VTEC acquired through a space division data selection strategy effectively reflects the ionosphere conditions at the altimetry IPP. After interpolation, the DORIS-based altimetry VTEC generally achieves an estimation that is 0.1 TECU smaller than that of GIM VTEC. Considering that all altimetry satellites are equipped with dual-frequency DORIS systems for POD, it should be practical to use DORIS ionospheric observations to obtain altimetry VTEC and assist in the satellite's altimetry applications. However, when the ionosphere is active, e.g. experiencing ionospheric storm phenomena, the ionospheric conditions at the DORIS IPP and

the altimetry IPP exhibit larger differences and lead to less accurate estimates of altimetry VTEC compared to those derived from GIM.

6.5 Summary of the Chapter

This chapter explored the feasibility of using DORIS observations to provide ionospheric delay corrections for single-frequency radar altimetry. The values of DORIS-based altimetry VTEC were calculated with various parameter settings. After finding the optimal parameters and related DORIS-based altimetry VTEC, we compared it with dual-frequency altimetry VTEC, which is considered the ground truth at altimetry IPP, and analyzed the RMS of the difference sequence. Additionally, GIM-based altimetry VTEC was also included in the comparison with dual-frequency altimetry VTEC, as GIM is widely used in ionospheric correction for single-frequency measurements, and its accuracy could serve as a benchmark for DORIS.

Throughout the computation process, we explored parameters related to data selection and interpolation methods. In the data selection phase, comparisons were made regarding elevation and the two methods for selecting neighboring altimetry IPPs, namely time division and space division. In terms of interpolation methods, both IDW and Kriging were employed and examined. After comparing the data coverage and accuracy for the parameters, a 10 degree elevation mask and the space division strategy were selected as the optimal parameter combination.

Finally, in the comparison between DORIS, GIM, and dual-frequency altimetry results, we found that under quiet conditions, the DORIS-based altimetry VTEC achieved a higher accuracy than GIM, making it a suitable method for providing ionospheric delay corrections for single-frequency radar altimetry. However, under active ionospheric conditions, the accuracy of DORIS-based altimetry VTEC was inferior to that of GIM, as .

7 Summary and Outlook

Altimetry satellites are widely used in Earth science research involving oceanography and glaciology. By measuring the signal's travel time, they can determine high-accuracy surface elevation information. However, as the signal propagates through the atmosphere, its interaction with charged particles in the ionosphere can affect the measurement accuracy. For dual-frequency altimetry satellites, such as Jason-3 and Sentinel-3, the ionospheric delay can be effectively eliminated by combining dual-frequency observations. However, for single-frequency altimetry satellites, or satellites that lost frequency in operation, it is necessary to correct ionospheric delay through alternative approaches.

Widely equipped on altimetry satellites, the dual-frequency DORIS receiver is a suitable method for ionospheric observation and correction. Firstly, the large frequency difference in DORIS signals makes the estimation of ionospheric delay less susceptible to external errors. Secondly, the DORIS ground segment, which transmits signals to the satellites, provides a global coverage of beacons for altimetry satellites including oceanic regions. In addition, due to the low orbit height of the altimetry satellites, the positions of the DORIS and altimetry IPP are spatially close for the same observation epoch. Given these advantages, this study explores the potential of using DORIS signals to provide ionospheric delay in altimetry observations.

The method of obtaining the ionospheric delay through dual-frequency DORIS observations is similar to that used in GNSS. However, in DORIS observations, the pseudo-range measurements suffer from an increased noise level, resulting in the DORIS carrier phase lacking an absolute level. Using data from Jason-3, this study utilized the IGS-provided GIM product to correct the unleveled data. The ionospheric level correction was performed at the highest elevation point of each DORIS pass, yielding leveled DORIS STEC values.

In this thesis, leveled DORIS STEC was compared with the IGS GIM STEC, and the RMS values of the differences were analyzed. The comparison revealed that passes with higher STEC values showed a larger RMS difference between DORIS and GIM. The daily average RMS in quiet ionospheric conditions was approximately 1.3 TECU, while in active ionospheric conditions, the difference increased to around 3.2 TECU. Additionally, as Jason-3 does not operate in a sun-synchronous orbit, the local time at the peak VTEC position shifts between 6:00 and 18:00 in different satellite revolutions.

Next, by applying a mapping function to convert DORIS STEC into DORIS VTEC, the ionospheric delay at the DORIS IPP can be obtained. To determine the DORIS-based altimetry VTEC, it is necessary to use different parameters to select DORIS VTEC values near the altimetry IPP and perform interpolation to attain DORIS-based altimetry VTEC. Since Jason-3 is equipped with dual-frequency altimetry signals, dual-frequency altimetry VTEC can be used as a reference to evaluate the accuracy of interpolation results for different parameter combinations. Specifically, this thesis examined different elevation cutoff angles and division strategies for the selection of DORIS VTEC. Here, the division strategies include space and time division, where data were chosen from a defined spatial or temporal vicinity around the altimetry IPP. For interpolation methods, inverse distance weighting (IDW) and Kriging interpolation were compared. After comparing both data coverage and accuracy, a 10-degree elevation mask was chosen, along with the selection of space division parameters. IDW interpolation method was then used to obtain the DORIS-based altimetry VTEC results.

Using these parameter selection methods, this study conducted an RMS value comparison between DORIS-based altimetry VTEC, GIM-based altimetry VTEC, and GIM-interpolated VTEC. In quiet ionospheric conditions, the DORIS-based altimetry VTEC showed an average RMS value advantage of 0.1 TECU over GIM-based altimetry VTEC over 30 days, given a 50% data coverage percentage. However, in more active ionospheric conditions, the DORIS results trailed by approximately 0.5 TECU compared to GIM. This difference can be attributed to two main factors: first, during active ionospheric periods, some observations were available only at a single frequency, thus reducing the amount of usable DORIS VTEC data; second, the active ionospheric activity caused the interpolated DORIS VTEC to represent the ionospheric delay at the altimetry IPP less accurately. Overall, in quiet ionospheric conditions, using DORIS VTEC for altimetry IPP ionospheric delay estimation offered smaller RMS than GIM, making it a viable option for ionospheric correction on single-frequency radar altimetry.

In summary, this study utilized the dual-frequency DORIS system aboard altimetry satellites to derive DORIS-based altimetry VTEC through spatial interpolation and analyzed its accuracy with GIM-based altimetry VTEC and dual-frequency altimetry VTEC. It was found that, during periods of quiet ionospheric conditions, DORIS-based altimetry VTEC achieved superior accuracy compared to GIM. However, in more active ionospheric conditions, the current data selection approach yielded DORIS-based altimetry VTEC with lower accuracy than GIM.

Future Research Directions

- Altimetry Corrections across Different Satellite Altitudes

This thesis primarily focused on the potential for altimetry corrections using observations from Jason-3. As a next step, accuracy analyses should be conducted on DORIS-based altimetry VTEC for satellites operating at different orbital altitudes, such as the lower-altitude Sentinel-3. This comparison will provide a broader understanding of DORIS applicability across varying satellite missions.

- Extended Temporal Analysis and Ionospheric Conditions

While this study analyzed the accuracy variation of DORIS products over two 30-day periods, future research should expand this time range. A longer analysis will allow for the identification of specific ionospheric conditions, such as F10.7 index thresholds, under which DORIS products outperform GIM products. Such findings can guide in selecting appropriate ionospheric correction products for single-frequency radar altimetry.

- Computation of GIM VTEC through Spherical Harmonic Coefficients

Due to the limited spatial resolution of GIM, this thesis performed grid-point interpolation of GIM at DORIS and altimetry IPPs. However, such interpolation reduces the accuracy of GIM products. Alternatively, it is possible to compute the corresponding VTEC directly at DORIS or altimetry IPPs using spherical harmonic coefficients provided by IGS. This direct computation of GIM VTEC not only has the potential to improve the accuracy of GIM-based altimetry VTEC but also could enhance the accuracy of GIM VTEC used as a reference in the leveling process for DORIS STEC.

- Data Coverage and Accuracy Enhancement

Future work should explore methods to simultaneously improve data coverage and accuracy. Key strategies include implementing more effective cycle slip detection to minimize the loss of valid ionospheric observations due to erroneous exclusions, and investigating variable DORIS selection strategies. For instance, as observed in figure 6.2, VTEC values can exhibit significant intra-day variability, even during active ionospheric conditions. Applying different window sizes to distinct sections of the

satellite ground track could enhance both the accuracy of DORIS corrections and the overall data coverage.

Another potential approach is the combination of different correction products. From the analysis in Chapter 6 on data coverage, it is evident that due to the distribution of DORIS stations and a limited number of observation data, the coverage of DORIS-based altimetry VTEC for altimetry IPP only reaches 50%. In contrast, GIM can provide ionospheric corrections for all altimetry IPPs. Therefore, future work should also aim to integrate both approaches and possibly other methods for observing the ionosphere to achieve larger coverage for single-frequency altimetry correction.

Bibliography

- [1] Mahdi Alizadeh, H. Schuh, Sonya Todorova, and Michael Schmidt. Global ionosphere maps of vtec from gnss, satellite altimetry, and formosat-3/cosmic data. *Journal of Geodesy*, 85, 12 2011. doi:10.1007/s00190-011-0449-z.
- [2] A. Auriol and C. Tourain. Doris system: The new age. *Advances in Space Research*, 46(12):1484–1496, 2010. doi:10.1016/j.asr.2010.05.015.
- [3] AVISO+ Altimetry. Frequencies used in altimetry. <https://www.aviso.altimetry.fr/en/techniques/altimetry/principle/frequencies-used.html>, 2024.
- [4] Saeed Bello, Mardina Abdullah, Nurul Shazana Abdul Hamid, and Bodo Reinisch. Comparison of ionospheric profile parameters with iri-2012 model over jicamarca. *Journal of Physics: Conference Series*, 852:012016, 05 2017. doi:10.1088/1742-6596/852/1/012016.
- [5] D. Bilitza and B.W. Reinisch. International reference ionosphere 2007: Improvements and new parameters. *Advances in Space Research*, 42(4):599–609, 2008. doi:10.1016/j.asr.2007.07.048.
- [6] Dieter Bilitza, Lee-Anne Mckinnell, Bodo Reinisch, and Tim Fuller-Rowell. The international reference ionosphere (iri) today and in the future. *Journal of Geodesy*, 85, 12 2011. doi:10.1007/s00190-010-0427-x.
- [7] Denise Dettmering, Marco Limberger, and Michael Schmidt. Using doris measurements for modeling the vertical total electron content of the earth. *Journal of Geodesy*, 88, 07 2014. doi:10.1007/s00190-014-0748-2.
- [8] Denise Dettmering, Michael Schmidt, Robert Heinkelmann, and Manuela Seitz. Combination of different space-geodetic observations for regional ionosphere modeling. *Journal of Geodesy*, 85:989–998, 12 2011. doi:10.1007/s00190-010-0423-1.
- [9] Denise Dettmering and Christian Schwatke. Ionospheric corrections for satellite altimetry - impact on global mean sea level trends. *Earth and Space Science*, 9(4):e2021EA002098, 2022. doi:10.1029/2021EA002098.
- [10] John Dow, R.E. Neilan, and Chris Rizos. The international gnss service in a changing landscape of global navigation satellite systems. *Journal of Geodesy*, 83:191–198, 01 2008. doi:10.1007/s00190-008-0300-3.
- [11] Lee-Lueng Fu and Anny Cazenave. *Satellite Altimetry and Earth Sciences: A Handbook of Techniques and Applications*. Academic Press Inc., 2001.
- [12] A. Goss, M. Schmidt, E. Erdogan, B. Görres, and F. Seitz. High-resolution vertical total electron content maps based on multi-scale b-spline representations. *Annales Geophysicae*, 37(4):699–717, 2019. doi:10.5194/angeo-37-699-2019.

- [13] S. Hilla. The extended standard product 3 orbit format (sp3-c). <http://igscb.jpl.nasa.gov/igscb/data/format/sp3c.txt>, 2010.
- [14] U. Hugentobler, M. Meindl, G. Beutler, H. Bock, R. Dach, A. Jäggi, C. Urschl, L. Mervart, M. Rothacher., S. Schaer, E. Brockmann, D. Ineichen, A. Wiget, U. Wild, G. Weber, H. Habrich, and C Boucher. Code igs analysis center technical report 2003/2004. In *IGS 2003-2004 Technical Reports*. IGS Central Bureau, 07 2008.
- [15] B. A. Iijima, I. L. Harris, C. M. Ho, U. J. Lindqwister, A. J. Mannucci, X. Pi, M. J. Reyes, L. C. Sparks, and B. D. Wilson. Automated daily process for global ionospheric total electron content maps and satellite ocean altimeter ionospheric calibration based on Global Positioning System data. *Journal of Atmospheric and Solar-Terrestrial Physics*, 61(16):1205–1218, November 1999. doi:10.1016/S1364-6826(99)00067-X.
- [16] John A. Klobuchar. Ionospheric time-delay algorithm for single-frequency gps users. *IEEE Transactions on Aerospace and Electronic Systems*, AES-23(3):325–331, 1987. doi:10.1109/TAES.1987.310829.
- [17] Attila Komjathy. *Ionospheric Effects on the Propagation of Electromagnetic Waves*, pages 286–291. 01 2014. doi:10.1007/978-0-387-36699-9_72.
- [18] F. Li and Michel Parrot. Study of the TEC data obtained from the DORIS stations in relation to seismic activity. *Annals of Geophysics*, 50(1):12 pages, 2007.
- [19] Feng Li and Michel Parrot. Study of the tec data obtained from the doris stations in relation to seismic activity. *Annals of Geophysics*, 50, 02 2007. doi:10.4401/ag-3086.
- [20] Zhenghang Li and Jingsong Huang. *GPS Surveying and Data Processing*. Wuhan University Press, 2000.
- [21] Marco Limberger. *Ionosphere modeling from GPS radio occultations and complementary data based on B-splines*. PhD thesis, Technische Universität München, 2015.
- [22] Ang Liu, Ningbo Wang, Denise Dettmering, Zishen Li, Michael Schmidt, Liang Wang, and Hong Yuan. Using doris data for validating real-time gnss ionosphere maps. *Advances in Space Research*, 72, 07 2023. doi:10.1016/j.asr.2023.01.050.
- [23] E. Lourme. Rinex doris 3.0. SALP-SP-M-EA-15578-CN, Issue 1.3, CNES, 2010. Accessed: 2024-11-22.
- [24] A. J. Mannucci, B. D. Wilson, D. N. Yuan, C. H. Ho, U. J. Lindqwister, and T. F. Runge. A global mapping technique for gps-derived ionospheric total electron content measurements. *Radio Science*, 33(3):565–582, 1998. doi:10.1029/97RS02707.
- [25] Flavien Mercier, Luca Cerri, and Jean-Paul Berthias. Jason-2 doris phase measurement processing. *Advances in Space Research*, 45(12):1441–1454, 2010. doi:10.1016/j.asr.2009.12.002.
- [26] Flavien Mercier, Luca Cerri, and Jean-Paul Berthias. Jason-2 doris phase measurement processing. *Advances in Space Research*, 45(12):1441–1454, 2010. doi:10.1016/j.asr.2009.12.002.
- [27] B. Nava, P. Coïsson, and S.M. Radicella. A new version of the nequick ionosphere electron density model. *Journal of Atmospheric and Solar-Terrestrial Physics*, 70(15):1856–1862, 2008. doi:10.1016/j.jastp.2008.01.015.

- [28] M. A. OLIVER and R. WEBSTER. Kriging: a method of interpolation for geographical information systems. *International journal of geographical information systems*, 4(3):313–332, 1990. doi:10.1080/02693799008941549.
- [29] Gérard Petit and Brian Luzum. IERS Conventions (2010). *IERS Technical Note*, 36:1, January 2010.
- [30] Todorova S, Schuh H, Hobiger T, and Hernández-Parajes M. Global models of the ionosphere obtained by integration of GNSS and satellite altimetry data. *Österreichische Zeitschrift für Vermessung und Geoinformation (VGI)*, 2:80–89, 2007.
- [31] Jerome Saunier. The doris network: Advances achieved in the last fifteen years. *Advances in Space Research*, 72(1):3–22, 2023. doi:10.1016/j.asr.2022.07.016.
- [32] Remko Scharroo and Walter H. F. Smith. A global positioning system-based climatology for the total electron content in the ionosphere. *Journal of Geophysical Research: Space Physics*, 115(A10), 2010. doi:10.1029/2009JA014719.
- [33] T. Schueler. On the interpolation of sp3 orbit files. Technical Report IFENTropAC-TN-002-01, Institute of Geodesy and Navigation, University FAF Munich, 1998.
- [34] Ashok Sharma, Onkar Gurav, Heramb Gaikwad, Gangadhar Chavan, Dada Nade, Suraj Nikte, Rupesh Ghodpage, and Parashram Tukaram. Study of equatorial plasma bubbles using all sky imager and scintillation technique from kolhapur station: a case study. *Astrophysics and Space Science*, 363, 03 2018. doi:10.1007/s10509-018-3303-4.
- [35] K. F. Tapping. The 10.7cm solar radio flux (f10.7). *Space Weather*, 11(7):394–406, 2013. doi:10.1002/swe.20064.
- [36] Parag Vaze, Steven Neeck, Walid Bannoura, Joseph Green, Angelo Wade, Michael Mignogno, Gerard Zaouche, Veronique Couderc, Eric Thouvenot, and Francois Parisot. The jason3 mission: completing the transition of ocean altimetry from research to operations. 10 2010. doi:10.11117/12.8685436.
- [37] Pascal Willis, Frank G. Lemoine, Guilhem Moreaux, Laurent Soudarin, Pascale Ferrage, John Ries, Michiel Otten, Jerome Saunier, Carey Noll, Richard Biancale, and Brian Luzum. The international doris service (ids): Recent developments in preparation for itrf2013. In Chris Rizos and Pascal Willis, editors, *IAG 150 Years*, pages 631–640, Cham, 2016. Springer International Publishing.
- [38] Yunbin Yuan, Ningbo Wang, Zishen Li, and Xingliang Huo. The beidou global broadcast ionospheric delay correction model (bdgim) and its preliminary performance evaluation results. *NAVIGATION*, 66(1):55–69, 2019. doi:10.1002/navi.292.